HIGH RESOLUTION ELECTRON MICROSCOPY AND X-RAY STUDY OF CANCRINITE

By

ISHMAEL HASSAN, B.Sc.

A Thesis

Submitted to the School of Graduate Studies

in Partial Fulfilment of the Requirements

for the Degree

Master of Science

McMaster University

January, 1980

THE SUBMICROSCOPIC AND AVERAGE STRUCTURES OF CANCRINITE

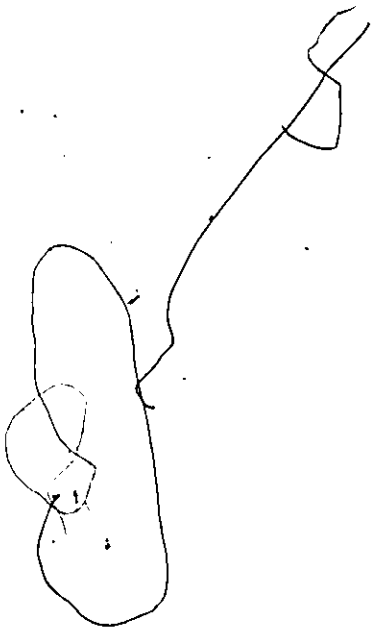

In Memory of My Brother

Kalamazad

MASTER OF SCIENCE (1980)
(Geology)

McMASTER UNIVERSITY
Hamilton, Ontario

TITLE: High Resolution Electron Microscopy and X-Ray Study of Cancrinite

AUTHOR: Ishmael Hassan, B.Sc. (McMaster University)

SUPERVISOR: Dr. H. D. Grundy

NUMBER OF PAGES: ix, 99

ABSTRACT

High resolution electron microscopy has provided information on the submicroscopic structure of a (Na, Ca) CO_3 cancrinite from Ontario and this information assisted in re-refining the average crystal structure (R = 2.9%) by standard X-ray techniques.

The superstructure of this mineral is commensurate and superlattice reflections can be indexed on a $8c_o$ - supercell. Six out of the seven such reflections have been observed by electron and x-ray diffractions. It is shown that the ordering of the CO_3 ions in the large channels is responsible for the superlattice reflections.

Furthermore, 'cancrinites' reported in the literature show superstructures that can be indexed on supercells of $5c_o$, $7c_o$, $8c_o$, $11c_o$, $14c_o$ and $16c_o$. The ordering of the CO_3 ions is again responsible for these extra reflections.

Moreover, the framework structures of three new mineral phases (liottite, afghanite and franzinite) that have recently been discovered are the same as that of cancrinite. They differ only as regards the intraframework anions (SO_4, CO_3 and Cl). The chlorine is statistically distributed with H_2O in the cages and the ordering of the SO_4 and CO_3 in the large channels gives rise to commensurate superstructure reflections which can be indexed on multiple subcells i.e., $3c_o$, $4c_o$, and $5c_o$ for liottite, afghanite and franzinite respectively.

In addition, losod and microsommite (or davyne) also fit within the framework of the proposed model. Losod can be considered as $2c_o$ -

cancrinite and microsommite whose a-dimension is twice that of cancrinite (but with the same c-dimension) can be considered as having different ordering in adjacent channels. However, superstructure data are not yet available for these minerals.

These new minerals should all be considered as "NC - cancrinite" as this term is necessary and sufficient to describe cancrinites. The value of N should be given on the basis of the multiple subcell observed.

ACKNOWLEDGEMENTS

I would like to express my gratitude to my supervisor Dr. H. D. Grundy for suggesting this project and for his productive suggestions and continuous support and encouragement throughout the preparation of this thesis. But most of all, for tolerating repeatedly over-optimistic reports about the project's progress and completion.

I also wish to express my appreciation to Dr. P. R. Buseck for making available the facilities at the Centre for Solid State Science at Arizona State University and Dr. I. MacKinnon and Mr. J. Wheatley of A.S.U. who gave invaluable assistance in sample preparation and in electron microscopy. Mr. J. Whorwood was most kind in preparing some of the more difficult photographs.

My sincere thanks to my wife Jackie, who contributed in many ways to the success of this project and also for her patience and support, and typing of this manuscript. Also thanks to Azar who made me look at my models from a lighter point of view.

Finally, I want to acknowledge the financial support of the Natural Sciences and Engineering Research Council of Canada and the Department of Geology, McMaster University for a Graduate Assistantship.

TABLE OF CONTENTS

LIST OF TABLES

LIST OF FIGURES

PLATES

CHAPTER 1

INTRODUCTION

The mineral cancrinite is a representative of the framework class of aluminosilicates; it is characterized by a variable content of water molecules, the large (alkali and alkali earth) cations (Na^+,K^+,Ca^{2+}) and anion groups (CO_3^{2-},SO_4^{2-},NO_3^-, including Cl and OH); this situation is reflected in the fact that the mineralogical literature (Edgar and Burley, 1963; Edgar, 1963; Deer, Howie and Zussman, 1966) gives a nonrigorous chemical formula for cancrinite, $(Na,Ca,K)_{6-8}(Al_6Si_6O_{24})(CO_3,SO_4,Cl,OH)_{1-2}\cdot 1\text{-}5H_2O$ (Deer, Howie and Zussman, 1966). The structure of cancrinite is characterized by six-membered $\{(Si,Al)_6O_{12}\}$ rings which are linked to form a continuous three-dimensional framework. The ring units give rise to hexagonal nets in a projection onto the (001) plane. The frameworks of the cancrinite minerals are commonly described by stacking sequences, that is, by the number of layers of six-membered rings in a particular sequence. Cancrinite has an AB stacking sequence, resulting in a 5.12Å c repeat. There is a whole family of related structures of chemical composition similar to that of cancrinite and in terms of stacking sequences, there is theoretically infinitely many different framework structures. Some very complicated stacking sequences of naturally occurring phases have been discovered recently (Table 1.1).

1.1 Statement of Problem

X-ray diffraction studies of cancrinite (Jarchow, 1965; Chen, 1970; Brown & Cesbron, 1973; Foit, Peacor & Heinrich, 1973) show diffuse

Table 1.1 Cancrinite Minerals

	a (Å)	c (Å)	Space group	Stacking sequence	Selected reference
Cancrinite	12.8	5.14	$P6_3$	AB	Jarchow (1965)
Microsommite	22.2	5.24	$P6_3$	AB	Klaska & Jarchow (1977)
Liottite	12.8	16.09	P6m2	ABABAC	Merlino & Orlandi (1977a)
Afghanite	12.8	21.35	$P6_3mc$	ABABACAC	Merlino & Mellini (1976)
Franzinite	12.8	26.58	P3m1	ABCABCBACB	Merlino & Orlandi (1977b)

Chemical Composition

Cancrinite $(Na,Ca,K)_{6-8}\ (Al_6Si_6O_{24})\ (CO_3,SO_4,Cl,OH)_{1-2}\cdot 1\text{-}5H_2O$

Microsommite $(Na_{3.23}Ca_{2.32}K_{1.92})_{TOT=7.47}\ (Si_{5.61}Al_{6.39})_{TOT=12}\ O_{23}\left[Cl_{2.25}(SO_4)_{0.39}\right]_{TOT=2.6}$

Liottite $(Ca_{10.76}Na_{9.29}K_{3.82}Fe^{3+}_{0.16})_{TOT=24.03}(Si_{18.34}Al_{17.66})_{TOT=36}O_{72}$
$\left[(SO_4)_{3.91}(CO_3)_{1.72}Cl_{2.61}(OH)_{3.58}\right]_{TOT=11.82}\cdot 1.83H_2O$

Afghanite $(Na_{19.44}Ca_{14.07}K_{2.73})_{TOT=36.24}(Si_{24.51}Al_{23.49})_{TOT=48.0}\ O_{102}\left[(SO_4)_{5.07}\right.$
$\left.Cl_{6.21}(CO_3)_{0.45}\right]_{TOT=11.73}\cdot 1.86H_2O$ (Bariand et al. 1968)

Franzinite $(Na_{21.53}Ca_{12.50}K_{5.22}Mg_{0.20}Fe^{3+}_{0.03})_{TOT=39.48}\ (Si_{31.32}Al_{28.68})_{TOT=60.00}\ O_{120}$
$\left[(SO_4)_{7.72}(CO_3)_{2.02}(OH)_{3.48}Cl_{0.59}\right]_{TOT=14.81}\cdot 4.31H_2O$

to strong non-Bragg reflections. These authors suggested that these satellite reflections are due to the intraframework cations and anions. However, Rinaldi and Wenk (1979) suggested that these reflections indicate a high density of stacking faults. Thus the cancrinite-related minerals appeared to be a good candidate for an investigation with the transmission electron microscope. In fact, recently such a study has been done, at relatively low resolution, on liottite, afghanite and franzinite (Rinaldi and Wenk, 1979). These authors were able to show (0001) stacking faults amd periodic superstructures in afghanite and franzinite and also satellites in the hko diffraction patterns of the latter.

In this study, a specimen of natural cancrinite from Dungannon Township, Ontario was studied by high resolution transmission electron microscopy (HRTEM) and X-ray diffraction (XRD). The specimen show strong superstructure reflections on precession photographs and hitherto, neither the origin of these superstructure reflections nor the detailed structure of cancrinite is known.

1.2 Previous Works

In the 1930s much work had been done on the structure of nosean (Pauling, 1930; Barth, 1932) and cancrinite (Pauling 1930, Kozu and Takane, 1933). The similarity between the two minerals has been noted by Gossner and Mussgnug (1930) before the structure of either had been worked out. They showed that if the c-axis of the hexagonal cancrinite was placed parallel to the $[111]$ axis of the cubic nosean and the a-axis placed parallel to the $[0\bar{1}1]$ axis of the cube the resulting cells have the same dimensions.

Similarity between the two structures exists. The structure of nosean looking down the $[111]$ axis consists of six-fold rings of alternating silicon and aluminum tetrahedra (Pauling, 1930). These rings are

12.78Å apart on a hexagonal cell, with the layers stacked in an ABC arrangement. The cancrinite structure looking down the c-axis consists of exactly similar layers of six-fold rings the same distance apart but stacked in an AB arrangement (Pauling, 1930). Kozu and Takane (1933) suggest a similar structure but with an AA arrangement giving rise to the space group $P6_3$.

Cancrinite from Blue Mountain, Ontario was studied by Phoenix and Nuffield (1949). They reported cell parameters and chemical analysis and suggest that some Al substitute for other cations because the sum of Al and Si was greater than 12, based on O=24. From density and charge considerations, they suggest that unfilled sites are common in cancrinite.

In 1955, P. Nithollon determined the structure of a cancrinite from Litchfield, Maine, based on the zeolite structure which consists of rings of six tetrahedra around the three-fold axes. The channels formed by the rings are occupied by H_2O, Ca^{2+} and CO_3^{2-}.

Most of the work done on cancrinite before 1955 has been of a crystallographic nature. However, in 1963, Edgar and Burley and in 1964, Edgar, synthesized various carbonate, bicarbonate and hydroxy cancrinites to determine their stability fields and breakdown products. They concluded that the chemical compositions of cancrinite controls their temperature stability and also their breakdown products.

Jarchow (1965) reported that $(Ca,Na)CO_3$ cancrinite from Litchfield, Maine show diffuse satellites on x-ray photographs. The satellites having indices $(hk\ell \pm 3/7)$. The crystal structure was determined from the relationships of the transformation hauyne to cancrinite. The structure was refined on three-dimensional data by the least-squares method to R = 0.089.

Chen (1970) studied cancrinites from Ontario and reported superstructure reflections that differ from one specimen to another with regard to their intensities, abundance and relative positions with respect to the main lattice reflections. In heated specimens, these satellite reflections decrease in intensities, shift in positions and streak parallel to a*.

Barrer et al. (1970, 1971) synthesized cancrinite in the sodalite crystallization field at 80°C by addition of sodium nitrate, chromate or molybdate and found that the crystals contain these salts as guest species in the place of the carbonate often found in natural cancrinite. They also attempted structure determinations for cancrinite nitrate ($R = 0.12$) and for a basic cancrinite (without CO_3^{2-}) ($R = 0.07$). In a separate study in 1971, Barrer et al. found that cancrinite hydrates take up substantial volumes of rare gases such as Ne, Ar, and Kr. These gases were trapped within the crystal when the temperature was lowered.

Brown and Cesbron (1973) and Foit et al. (1973) studied cancrinites from different sources, found superstructures characterized by values of c parameter equal to $5c_o$, $11c_o$, $16c_o$ and $21c_o$ where $c_o = 5.13$Å. Some of these values are questionable and will be discussed in section 6.1 where the data are reexamined. The diffraction pattern of all these cancrinites differ as regards the satellite reflections but do not differ in the positions and intensities of the sharp spots. The authors suggested that "cancrinites" have the same aluminosilicate framework structure, differing only in the ordering of the cations outside the framework, which leads to the appearance of the satellite reflections. Or alternatively the satellite reflections are due to stacking faults (Rinaldi & Wenk, 1979).

Even though 3-dimensional data refinements for cancrinite have been reported by Jarchow (1965) and Barrer et al. (1970), it should be noted that these refinements are poor ($R \geq 7\%$). They reported quite large temperature factors for the intra-framework cations and anion groups. Furthermore, the amount of these ions reported in the chemical analyses are less than that required by symmetry ($P6_3$).

1.3 Crystal Structure of Cancrinite

The three-dimensional framework structure is uniquely accepted (Jarchow, 1965; Barrer et al. 1970), but the location of the alkali (alkali earth) cations and the anion groups is still a subject of controversy.

The crystal structure of cancrinite, space group $P6_3$, a = 12.75, c = 5.14Å, was determined by Pauling (1930) and refined by Jarchow (1965).

The rigid three-dimensional framework (composition $Al_6Si_6O_{24}$) of cancrinite has an ordered disposition of $(Si,Al)O_4$ tetrahedra (Jarchow, 1965; Barrer et al., 1970) and three different kinds of channels when viewed down the c-axis: (1) A wide channel system along the 6_3 axes. These channels are circumscribed by puckered twelve-member rings with free diameter ~8.7Å. (2) A smaller channel system along 3-fold axes. These channels are circumscribed by six-member rings of ~5.2Å free diameter. (3) A still smaller channel system consisting of four-member rings. The main 12-ring channels are surrounded by six 6-ring channels and six 4-ring channels (Fig. 1.1).

Two types of non-intersecting channels can be seen in the cancrinite structure when it is viewed down the a-axis i.e. a*-c* section, (Fig. 1.2). These are double sets of 6-member rings separated by 4-member rings.

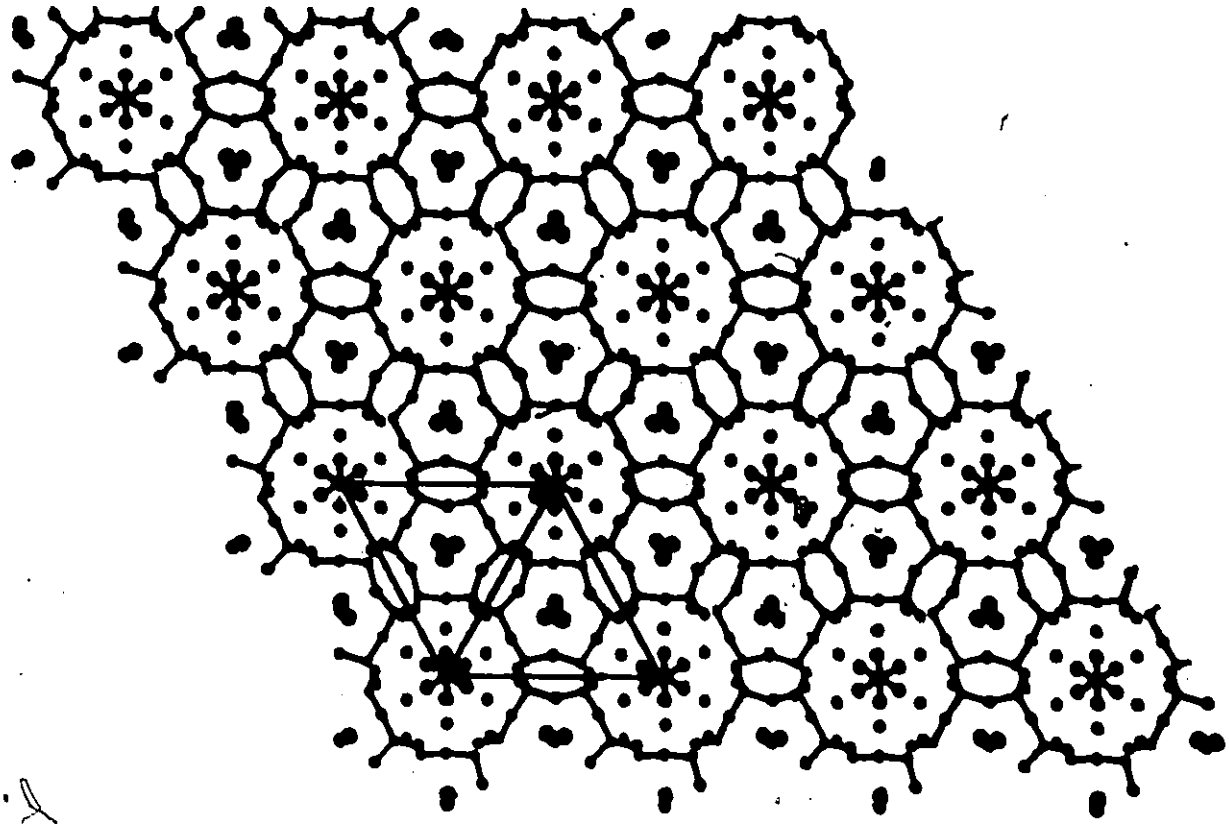

Figure 1.1: The structure of cancrinite view down the c-axis showing the three different non-intersecting channel systems. The main 12-ring channels are surrounded by six 6-ring channels and six 4-ring channels. A unit cell is outlined. Atoms are identified in Figures 1.4 and 1.5. (ORTEP, Johnson, 1965; Data from Jarchow, 1965).

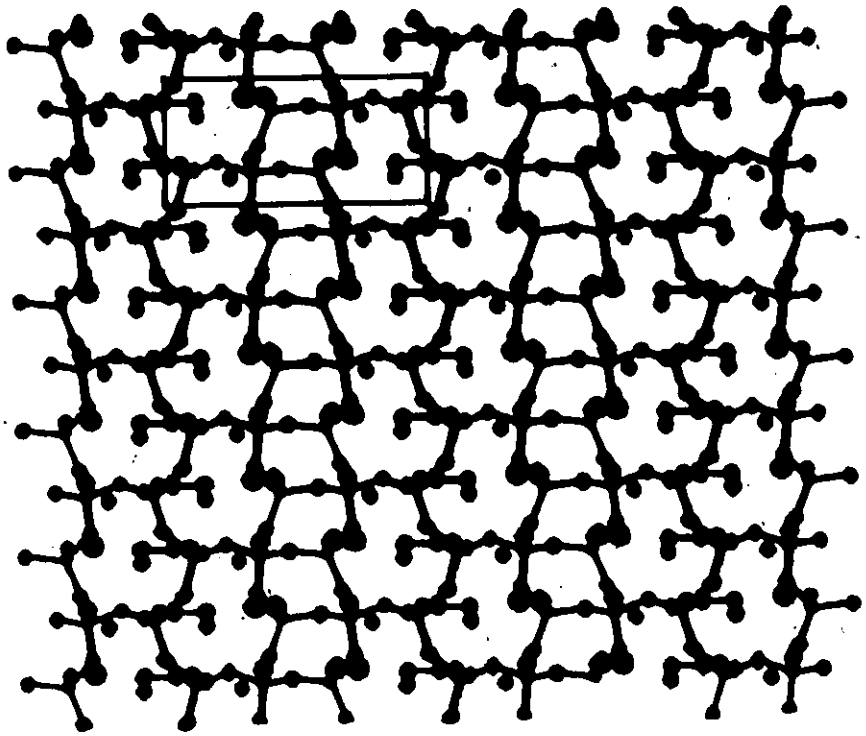

Figure 1.2: The structure of cancrinite view down the a-axis (a^*-c^* section) showing the two different non-intersecting channel systems. These are double sets of 6-member rings separated by 4-member rings. A unit cell is outlined. (ORTEP, Johnson, 1965; Data from Jarchow, 1965).

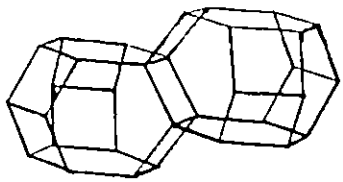

Figure 1.3: 11-hedral cancrinite cages, showing method of linkage. (After Barrer et al., 1970).

The hexagonal cancrinites framework can readily be envisaged as the result of stacking in an ABAB . . . sequence identical layers of linked 6-rings: each ring is linked to three rings in the preceding layer and to three other rings in the succeeding one. Figure 1.3 shows the method of linkage, giving rise to small cages and the cages' distorted six-ring opened windows. The ABAB . . . stacking sequence gives a system of three types of non-intersecting channels, parallel to the c-axis (Fig. 1.1). However, stacking faults, in which occasional ABC layer sequence interrupt the AB sequence in ideal cancrinite, can block the wide channels by having 6-ring channels coincident with the large channels, (Barrer et al. 1970; Brown & Cesbron, 1973; Foit, Peacor & Heinrich, 1973).

Positions of Cations and Anions

The ideally ordered $(Na,Ca)CO_3$ cancrinite unit cell may accommodate $2H_2O$, $2CO_3$, and Na and Ca atoms in two equipoints of rank 6 and 2 respectively to account for $P6_3$ space group (Foit et al., 1973). However, in natural cancrinite there tend to be excess and/or deficiency for some of the intraframework molecules, cations and anion groups indicating that the space group $P6_3$ is pseudo-space group of cancrinite.

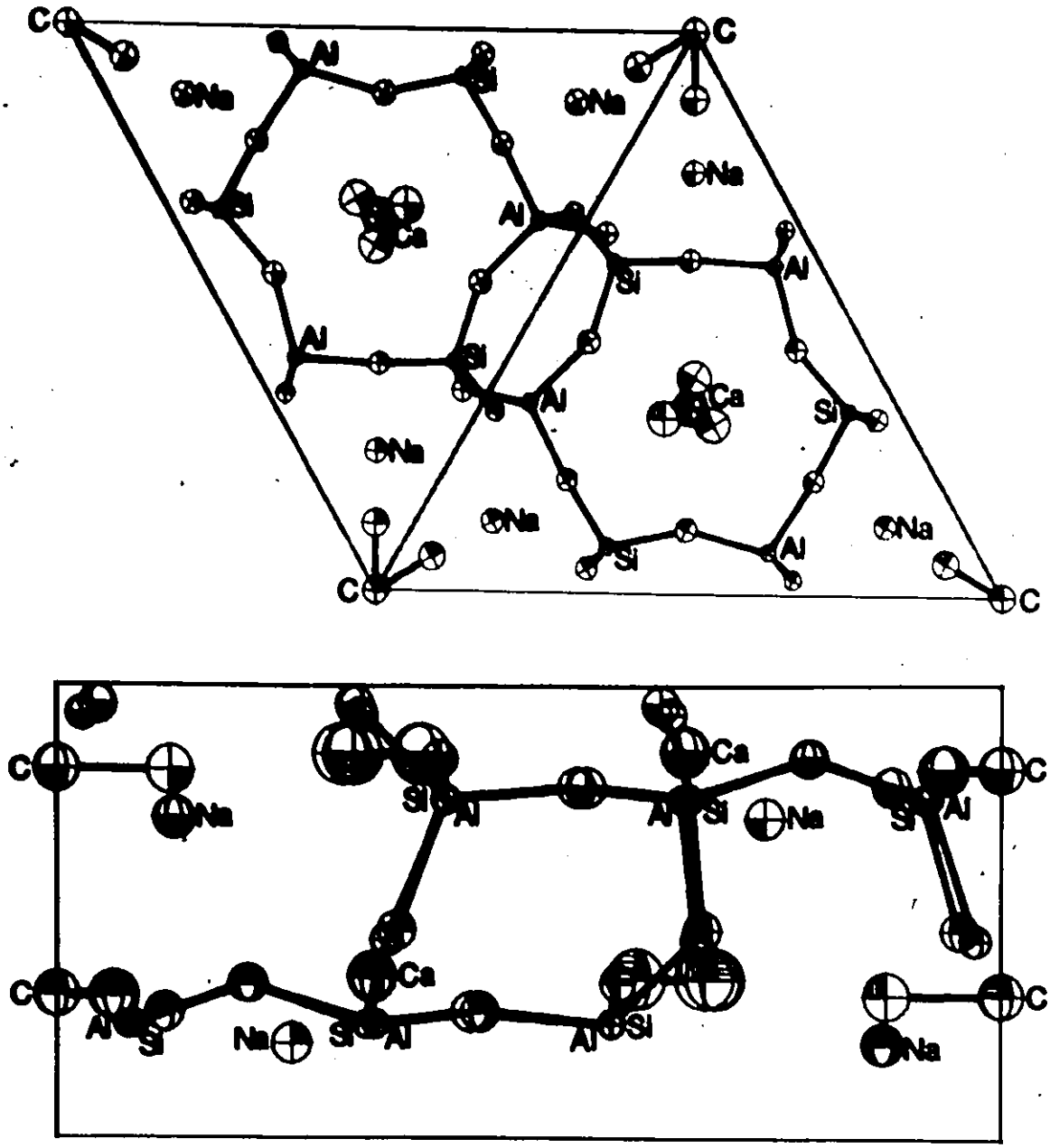

Figure 1.4: (Top) A unit cell of cancrinite (cell edge a=12.75Å) view down the c-axis.

Figure 1.5: (Bottom) A unit cell of cancrinite view down the a-axis (C=5.14Å; 1/a*=11.04Å). The oxygen of H_2O is disordered over three slightly different positions and they project on the Na (unlabelled) atom in the cage. Na and Ca are statistically distributed. Oxygen atoms are unlabelled and hydrogen atoms are not shown. (ORTEP, Johnson, 1965; Data from Jarchow, 1965).

Jarchow showed that Na^+ and Ca^{2+} cations occupy both of two kinds of channels aligned parallel to the 6_3 and 3-fold axes. The cations in the main channel are in front of the distorted six-ring windows opening to the cages. They spiral down the main channels. Those cations along the 3-fold axes are at different fractions of heights of the unit cell. The H_2O molecules are in the cages (1 molecule in each cage) on 3-fold axes while calcium carbonate salts are in the main channels. Figures 1.4 and 1.5 show the cation positions when viewed down the c-axis and down the a-axis respectively. Barrer et al. (1970) found similar ion sites for cancrinite as Jarchow. However, for "basic" cancrinite (without CO_3^{2-}), the site found by Jarchow in front of the 6-ring opening to the main channel (Jarchow's $Na_2(Ca)$ site) is divided into two positions Na(1) and Na(2). Also, they placed the two water molecules in the main channels rather than in the cages.

CHAPTER 2

TRANSMISSION ELECTRON MICROSCOPY (TEM)

Since the early 70s, transmission electron microscopy (TEM) has added numerous important new data to mineralogy and has considerably changed its outlook. This is partly due to the fact that metallurgists and crystal physicists have begun to show a greater interest in the complicated structures of minerals, and partly to recent improvements in experimental techniques, mainly the availability of ion-thinning devices and increasing resolution in the electron microscope. While electron microscopists have become increasingly interested in minerals, mineralogists have realized advantages of the new technique and have applied it with increasing frequency.

Before this new era, mineralogists have been mainly accustomed to two classical tools i.e. the polarizing microscope and x-ray diffraction techniques. With the optical microscope we are able to determine the morphology and optical properties; we can see twins and exsolution lamellae which are larger than the wave length of light. From x-ray diffraction data we can derive accurately the position of atoms in the unit cell on the scale between 100 and 10,000Å. However, such a crystal structure determination gives us an average over many thousands of unit cells and assume that the cells are identical.

Increasingly important to the mineralogist are the important structures contained in minerals on the scale 1 - 100Å, which could not be directly imaged with conventional techniques. Furthermore, crystals

are not perfect but contain defects at the unit cell scale. The electron microscope is the ideal instrument to investigate this range of inhomogenities in minerals which also contain important geological information on parameters describing the cooling history of minerals and rocks and on the conditions of deformation (Wenk, 1976).

Since images obtained with the electron microscope are related to structures determined from x-ray studies, it is interesting to compare TEM with x-ray diffraction a little more closely.

2.1 TEM vs X-ray Diffraction

TEM	XRD
1. Electrons are scattered by electrostatic potential field. Thus scattering by an atom involves both its nucleus and its electrons.	1. X-rays are diffracted mainly by the orbital electrons.
2. Since an electron beam consists of changed particles, high beam intensities can be focused to a small spot (or very small area) by electromagnetic lenses.	2. X-rays cannot be focused.
3. The wavelength of electrons typically used for transmission electron microscopy have $\lambda = 0.037$Å. Thus the Bragg angle, θ, is much smaller leading to an increase in the number of planes that simultaneously fulfill the Bragg condition.	3. For x-rays CuK_α have $\lambda = 1.54$Å, nearly two orders of magnitude greater. Therefore, the Bragg angle, θ, is much larger. Fewer planes fulfill Bragg condition. The radius of the Ewald sphere is smaller and one must go to

Furthermore the radius of the Ewald sphere is larger and its surface more closely approaches a plane and thus can more nearly coincide with a plane of the reciprocal lattice.

4. Physics of electron diffraction is more complicated since interactions of the electrons with atoms is much stronger. Thus double or multiple diffraction of the electrons commonly produces some "forbidden" reflections. This becomes a serious problem for thick specimens. Another problem is the effect of absorption produced by inelastic scattering. The combined effect of the above factors makes the interpretation of electron diffraction patterns difficult. Thus a dynamic treatment for diffraction is required.

5. The electron diffraction patterns are immediately visible on a fluorescent screen.

6. Electron diffraction patterns are easily obtained from very small specimens (~1 μm diameter).

complicated precession motions to obtain similar planes of the reciprocal lattice.

4. Physics of x-ray diffraction is less complicated since the interaction of x-rays with atoms is less strong so one uses a kinematical treatment.

5. Diffraction patterns require extended photographic exposures.

6. Need larger specimens.

7. Electron images can be obtained from the diffracted beams.	7. Images cannot be obtained from diffracted beams.
8. The data are not averaged over nearly as many unit cells as for x-rays. The difference in volumes studied is at least 14 orders of magnitude! One can observe point to point resolution of 3Å (intermediate between bond length and unit cell dimensions) and consequently observe deviations from ideal structures. Thus the great single advantage of EM is the ability to observe localized fine details.	8. Data are averaged over many unit cells. Thus the great advantage of x-rays is the ability to average structure over relatively large volumes.
9. The images observed by TEM are to a first approximation related to the corresponding electron diffraction patterns through their Fourier transforms.	9. X-ray diffraction pattern is the Fourier transform of the electron density.
10. Can obtain images of sets of unit cells as well as some of the details within individual unit cells.	10. There is no way that direct visual images of mineral structures can be obtained.

We can clearly see that EM has distinct advantages over X-ray diffraction but it must be kept in mind that for all quantitative calculations in EM the crystal structure must in principle be known first and therefore EM does not replace X-ray diffraction studies. On

the other hand there are many examples where electron microscopic evidence was instrumental in the interpretation of X-ray data (Wenk, 1976). The two techniques ideally complement each other.

2.2 Fundamentals of EM

The information that is obtained by electron microscope methods is derived from the scattering processes that take place when the electron beam travels through the specimen. The two main types of scattering are: (1) elastic -- the interaction of the electrons with the effective potential field of the nuclei, involving no energy losses and which can be coherent or incoherent, and (2) inelastic -- the interaction of the electrons and the electrons in the specimen involving energy losses i.e. absorption. It is the elastic scattering that produces a diffraction pattern; and if the scattering centers in the specimen are arranged in an orderly, regular manner such as in crystals, the scattering is coherent and results in spot patterns, Kikuchi patterns and, if the sample is a fine-grained polycrystal, ring patterns.

The basic reason for the utilization of the electron microscope is its superior resolution resulting from the very small wavelengths of electrons compared to other forms of radiation for which an optical system can be constructed. The resolution is given by the Rayleigh formula which is derived by considering the maximum angle of electron scattering (α) which can pass through the objective lens. This formula is:

$$R = \frac{0.61\lambda}{\alpha} \qquad (1)$$

where R is the size of the resolved object, λ is the wavelength, and α is identical to the effective aperture of the objective lens.

In the electron microscope, the effective aperture is limited chiefly by spherical aberration. The spherical aberration error is:

$$\Delta S = C_s \alpha^3 \qquad (2)$$

where C_s is the coefficient of spherical aberration of the objective lens ($\simeq$ focal length e.g. 3mm).

Therefore, R increases with decreasing α ; whereas ΔS decreases with decreasing α. Thus, one arrives at an optimum aperture and minimum resolution given by:

$$\alpha_{opt.} = A(\lambda^{\frac{1}{4}}) C_s^{-\frac{1}{4}}, \qquad (3)$$

$$\Delta R_{min} = B(\lambda^{3/4}) C_s^{\frac{1}{4}}, \qquad (4)$$

where A and B are constants of order 1.

The relativistic wavelength of electrons depends on the accelerating voltage and is given by the modified De Broglie wavelength:

$$\lambda = h \,/\, (2m_o eE(1 + eE \,/\, 2m_o c^2))^{\frac{1}{2}} \qquad (5)$$

$$= 12.26 \,/\, E^{\frac{1}{2}} \,(1 + 0.9788 \times 10^{-6} E)^{\frac{1}{2}} \ (\text{Å}) \qquad (6)$$

where h = Planck's constant, m_o is rest mass and e the change of the electron, E is the accelerating potential (volts), and c is the velocity of light. Thus when E = 100kV, λ is 0.037Å, $\alpha_{opt} \simeq 6 \times 10^{-3}$ rad and $\Delta R_{min} \simeq 6.5$Å for C_s 3.3mm.

Another advantage of the small wavelength of electrons is that the depth of field and depth of focus are very large in electron microscopes.

2.3 Electron Diffraction and Imaging

The essential stages in the formation of an image in an electron microscope can be described in terms of the Abbe Theory of the formation of the image by the objective lens. That is, the image is to a first approximation related to the corresponding electron diffraction pattern through Fourier transforms. This wave theory can be illustrated by reference to the geometric optics diagram, Figure 2.1, which shows that the image is a magnified picture of a diffraction spot selected by the aperture in the back focal plane of the objective lens. The intermediate lens can be focussed at the back focal plane of the objective thereby allowing the diffraction pattern to be observed on the screen and photograph. If an aperture with diameter D is placed in the image plane, only electrons passing through an area D/M on the specimen can reach the final screen. (M = objective lens magnification).

For a parallel incident beam the amplitude distribution at the exit face of a thin crystal is given by the transmission function $f(x,y)$, where x and y are the Cartesian coordinates for all points on the crystal, relative to a set of arbitrary axes.

In very thin objects the lateral spread of the electron wave due to Fresnel diffraction effects may be neglected and the electron wave may be considered to travel straight through the object, suffering only a phase change proportional to the electrostatic potential it has experienced along a straight-line path. The object is therefore a phase object with transmission function

$$f(x,y) = e^{-i\sigma\phi(x,y)} \qquad (7)$$

where σ is the interaction constant ($\sigma = \pi/\lambda E$; λ is the wavelength and E

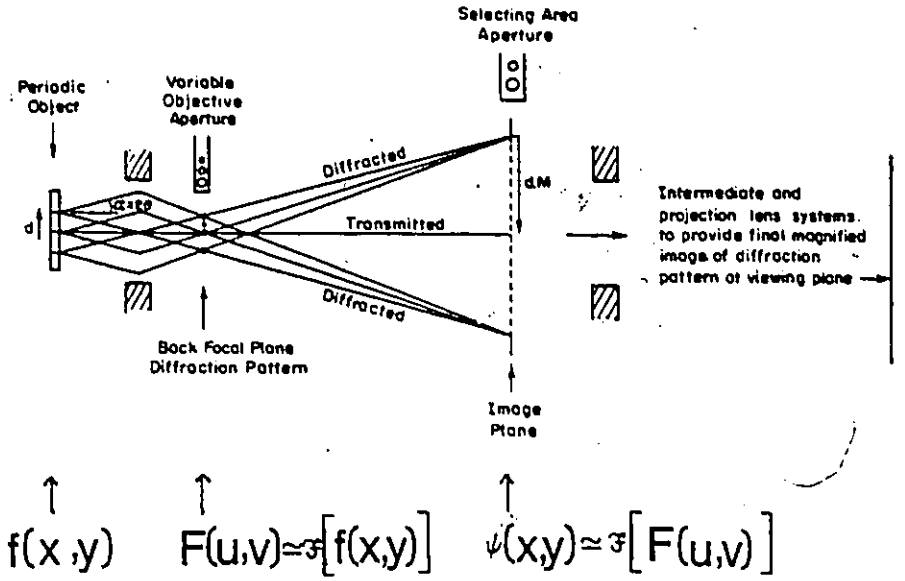

Fig. 2.1: Phase contrast imaging from a periodic object. The diffraction pattern is formed in the back focal plane. The period d is imaged as magnified fringes if the diffracted and transmitted beams recombine at the image plane (when $2\theta \leq \alpha$). Notice the inversion between diffraction pattern and image relative to the object. The mathematical functions appropriate to the various positions are indicated; see text for details. (After Van der Biest and Thomas, 1976).

is the accelerating potential) and $\phi(x,y)$ is the projection of the three-dimensional electrostatic potential distribution within the thin crystal, along the electron beam direction, defined to be the z-axis. All the variables in equation (7) are in general known and hence $f(x,y)$ can be evaluated.

From Figure 2.1, we see that all radiation scattered at a particular angle from the object is brought together at one point in the back focal plane of the objective lens. The amplitude distribution $F(u,v)$ in this back focal plane is the Fraunhofer diffraction pattern

of the object and is calculated by taking the Fourier transform of the transmission function f(x,y):

$$F(u,v) = \mathfrak{F}(f(x,y)) \qquad (8),$$

analogous to the x-ray diffraction pattern being the Fourier transform of the electron density. Under ideal conditions, the formation of the image in the Gaussian image plane of the objective lens can be regarded as a further process of Fraunhofer diffraction, described by the Fourier transform:

$$\psi(x,y) = \mathfrak{F}\left[F(u.v)\right] = f(-\frac{x}{M}, -\frac{v}{M}) \qquad (9),$$

since the transform of the transform is the original function. Hence the lens, ideally, takes the radiation transmitted and scattered from each point of the object and brings it together with the correct relative phase to form the amplitude wave function, $\psi(x,y)$, i.e. the lens recreates the transmission function of the object, inverted and magnified by a factor M. We can refer the image to the scale of the object and write instead,

$$\psi(x,y) = f(x,y) \qquad (10).$$

Due to several instrumentally introduced effects, the image cannot be considered as a simple Fourier transform. Thus, the diffraction function, F(u,v), is modified by a phase term, $e^{i\chi}$, and an objective aperture function A(u,v), so the resulting relationship takes the form

$$\psi(x,y) = F(u,v) \cdot e^{i\chi} \cdot A(u,v) \qquad (11).$$

The phase term, $e^{i\chi}$, is introduced by spherical aberration of the objective lens and optical defocussing. For a given set of operating conditions χ is constant and can be evaluated.

The objective aperture function, A(u,v), is the result of the insertion of a screen with a hole ($\sim 50\mu m$ diameter) centred about the incident electron beam to stop high order diffracted beams from contributing to the image, as they suffer increased phase change. The value of A(u,v) is 1 for each beam that is allowed to pass through the aperture and 0 for those beams that are blocked.

The expression for the image at optimum defocus can now be determined by taking the Fourier transform of the corrected diffraction function. The resulting expression for the intensity, I(x,y), in the image plane is

$$I(x,y) = \psi\psi^* \simeq 1 + 2\sigma\phi(x,y), \qquad (12)$$

where $\phi(x,y)$ is the projection of the three-dimensional electrostatic potential distribution within the crystal, along the beam direction. The intensity distribution (image contrast) in the electron micrographs of crystal structures have been shown to be approximated by equation (12) (Cowley and Iijima, 1972; Allpress and Sanders, 1973; Cowley and Iijima, 1976). Consequently, using electron microscopy we can see the projected structure directly.

Since contrast observed in the electron image derives from electrostatic potential differences in the crystal, then columns of heavy atoms or dense rows or other regions of high electrostatic potential appear dark and low atomic number atoms or regions appear light. In the case of a mineral which contains only light elements, the contrast in the electron image is developed between empty channels and the surrounding atoms, as in the case of beryl (Buseck and Iijima, 1974) and cancrinite, to be presented in this report.

2.4 Calculated Images for HRTEM

The use of the transmission electron microscope to obtain high resolution images which show structure within the unit cells of minerals and synthesized crystals, is one of the more interesting recent developments in solid state science. However, the interpretation of such images has, on occasion, been a subject of controversy because a given crystal can produce a variety of images, depending on parameters such as the objective aperture, crystal thickness and the value of defocus of the objective lens. Such controversies can be resolved since it is now possible to produce calculated images of a given (or trial) structure and obtaining matches of these with experimental images (O'Keefe, Buseck and Iijima, 1978).

Recently, a computer program has been developed at Arizona State University (Fejes, 1973; Skarnulis, 1975) and it can be used to calculate the images expected from a given model structure. The program uses the Cowley-Moodie multislice formulation (Cowley and Moodie, 1957) and considers effect of dynamic diffraction; specimen parameters such as thickness and orientation; microscope parameters such as size of objective aperture, accelerating voltage, objective lens defocus and aberrations, and the finite illuminating angle produced by the condenser lens. With the use of this program, problems of ambiguity in interpreting HRTEM images can be minimized by computing images for various operating conditions and obtaining matches of these computed images with experimental ones.

In view of the importance of computed images as an aid in interpreting structure images obtained experimentally, the physical principles involved will be summarized.

In principle, the Cowley-moodie multislice formulation deals with multiple scattering within a crystal by dividing the crystal into slices of such thickness that multiple scattering within each slice can be neglected. The wave amplitude scattered by each slice can then be represented as:

$$\psi(x,y) = \exp i\sigma\phi(x,y)\ \Delta z \qquad (13)$$

where $\psi(x,y)$ is the wave amplitude, Δz is the slice thickness and σ is the interaction parameter defined as:

$$\sigma = \frac{2\pi}{\lambda E}\ \frac{1}{1 + (1 - v^2 / c^2)^{\frac{1}{2}}} \qquad (14)$$

where λ is the electron wavelength, E the accelerating potential, v the electron velocity and c the velocity of light. The slices are represented by planes, separated by vacuum gaps, the emergent wave amplitude being calculated by allowing for successive interactions of the wave-front with each plane in turn, followed by propagation across the vacuum gap to the next slice and so on. Therefore, $\psi_1(x,y)$, the wave amplitude immediately following the first plane, after propagation across the gap to the next plane, is of the form:

$$\psi_1'(x,y) = \exp\ i\sigma\phi(x,y)\Delta z * \exp\frac{2\pi i}{\lambda}\left\{(\Delta z^2+x^2+y^2)^{\frac{1}{2}} - \Delta z\right\} \qquad (15)$$

where * signifies convolution. After the second plane, the wave front becomes:

$$\psi_2(x,y) = \psi_1'(x,y) \exp i\sigma\phi(x,y)\ \Delta z \qquad (16)$$

Hence, the wave amplitude, after the n^{th} plane can be written in terms of that after the $(n-1)^{th}$ plane as:

$$\psi_n(x,y) = \left\{ \psi_{n-1}(x,y) * \exp\frac{2\pi i}{\lambda} \left\{ (\Delta z^2+x^2+y^2)^{\frac{1}{2}} - \Delta z \right\} \right\} \exp i\sigma\phi(x,y)\,\Delta z \qquad (17)$$

In this way the emergent wave-front can be written in terms of that on the first plane and the number of individual operations depend on the number of slices into which the crystal is initially divided. This method is quite suitable for computation and, once established, can be used as a routine technique for calculating the image features generated by a given (or trial) structure.

For cancrinite the slice thickness was limited to 5.14Å and 12.75Å for calculations down c- and a-axis respectively. The emergent wave amplitudes was calculated for specimen thickness ranging to about 100Å. After modifications by the phase contrast function (Erickson and Klug, 1971) and aperture function, the amplitudes were Fourier transformed to produce theoretical ($0k\ell$) and ($hk0$) images. Defect of focus (defocus) was sampled at intervals of 100Å in the region from +600 to -1500Å. The region of -800 to -1200Å is particularly important for image interpretation in terms of projected structure, because, at these values of underfocus, approximately equal instrumental phase shifts occur in all the diffracted beams contributing to the image (Mallison, et al., to be published). The objective aperture radius in reciprocal space and the coefficient of spherical aberration (C_s) are dependent upon the focal length of the objective lens, which in turn varied with specimen height. Images were calculated for a number of objective aperture radii to obtain a realistic radius that does not eliminate important diffracted beams. This radius was found to be $0.308Å^{-1}$ (resolution = 3.2Å) and it agrees quite well with

that obtained from the diffraction pattern (radius = 0.42 Å^{-1}). Trial calculations involving increases in objective lens spherical aberration and compensation for chromatic aberration indicated that these factors had little effect upon image contrast with the aperture size employed. All calculations were carried out on an IBM computer at McMaster University Business Centre.

CHAPTER 3

EXPERIMENTAL

3.1 Sample Preparation

Specimens were prepared by two different methods for electron microscopic investigation. Small fragments were removed from each specimen, embrittled by imersion in liquid nitrogen and crushed under acetone to a fine powder in an agate mortar. The powder was then suspended in chloroform or acetone by ultrasonic dispersion and a drop of the specimen was deposited on holey carbon grids. Specimens prepared in this way gave many small wedge-shaped crystals, with edges sufficiently thin to produce lattice images when the crystals lay over holes in the support film. Due to extensive radiation damage suffered by cancrinite, particularly the a*-c* section, the crushed sample method of obtaining images was quite tedious. It requires orientation and recording of images to be done in a very short time. However some images were obtained by this method mainly by using the part of the crystal fragment that lies on the carbon film for orienting the zone axis of interest parallel to the electron beam and "sneaking up" on the undamaged part of the crystal that overlap the carbon film and photographing the image within a few seconds. The radiation damage of cancrinite is so rapid that a defocus series was not possible to obtain from any particular area of a crystal and often only a few usable images were obtained from a crushed fragment.

This tedious and laborious task of obtaining images from crushed fragments was particularly overcome by using ion-thinned specimens, which

contained very large thin areas in approximately the same orientation. The samples were examined in hand specimen and by recognition of cleavage faces were cut and made into petrographic thin-sections whose normals are close to the zone axes of interest. A copper-slotted grid was glued onto the thin-section using an Eastman 910 adhesive. (This adhesive bonds rapidly, is non-soluble in acetone and the bonds do not break on heating. The epoxy cement for making the thin-section is soluble in acetone and the bonds are easily broken on heating). The specimen, after bonded to the grid, was cut into a disc of the same size as the grid, using a diamond knife. The thin-section was then placed on a hot plate and after the epoxy bonds were broken, the grid was removed and cleaned in acetone, which essentially gets rid of the epoxy. The thin section was also removed from the hot-plate and saved for making more grids, if necessary. The specimen was then placed in an ion-thinner and thinned by argon ion bombardment for about 12-18 hours.

Even though very large thin areas in approximately the same orientation were obtained by making ion-thinned specimens, the "sneaking up" method, described earlier, was used to photograph images, as cancrinite suffered rapid electron beam damage. Unfortunately, even though this method produced a few good images, the majority of images obtained are poor, since no time is allowed for cessation of stage drift. Furthermore, as two different sample preparation techniques were employed, and similar results were obtained with samples prepared by each method, the observed microstructures are not related to sample preparation. This is also confirmed by matching computed and experimental images.

3.2 Electron Microscopy

All specimens were examined in a JEM 100B microscope equipped with a modified top-entry goniometer stage, extra anti-contamination devices and a non-conventional high-magnification intermediate lens (Buseck and Iijima, 1974). The high resolution goniometer stage combines a 180° rotation and a ± 30° tilt from the horizontal for obtaining the proper orientations of the crystal. Before tilting, the orientation of the specimen should lie within the 30° of the desired zone axis relative to the electron beam.

Good structural information is obtained from specimens whose thickness do not exceed ≃ 150Å. Therefore, one must locate a crystal of suitable thickness and proper orientation for studying particular features of interest.

The microscope was operated at an accelerating potential of 100kV. All photographs were obtained by imaging the beams passed by a 50 μm diameter objective aperture centered about the incident beam. The 50 μm diameter corresponds to a radius of ≃ $0.42 Å^{-1}$ in the electron diffraction pattern. The diameter of the condenser aperture was 150 μm and initial magnifications ranged from 200,000 to 500,000 times.

Optimum images for structural detail should be obtained at a critical value of underfocussing of approximately 900Å relative to the Gaussian image plane. To ensure that the optimum image is viewed, a through-focus series of images are usually recorded under various focussing conditions. Since cancrinite damages rapidly in the electron beam, a through-focus series was not obtained, rather many images were

obtained for different experimental conditions at different sections of the crystal and these images are matched with the calculated images to select a few images that best represent the projection of the cancrinite structure.

3.3 Electron Diffraction Patterns

A suitable crystal fragment, or, in the case of ion-thinned specimens, a suitable part of the crystal, must be located to produce a lattice image. Once located, the crystal must be tilted and rotated to obtain the appropriate zone axis parallel to the electron beam. The zone axis and the electron beam should be within 0.5° to produce good lattice images. In the case of a zone axis $[uvw]$, parallel but in opposite sense to the electron beam, reflections hkl that satisfy the criterion $hu+kv+lw=0$ will appear. For example, for $[100]$ coincident with the electron beam, the set of reflections okl will be in a proper Bragg diffraction position. For the cancrinite samples studied, two major zone axes were set coincident with the electron beam. These are firstly, the c-axis, $[001]$, having the hko set of reflections in the proper Bragg diffraction position and secondly, the a-axis, $[100]$, having the okl set of reflections in the proper Bragg diffraction position. In these two orientations the images could readily be interpreted in terms of the projected charge density (PCD) approximation (Lynch, Moodie and O'Keefe, 1975).

Correct orientation is obtained by viewing the diffraction pattern during tilting and rotation. The orientation is judged correct if pairs of diffraction spots on opposite sides of the incident beam are of equal intensity. In the diffraction mode, during tilting and rotation the

crystal can easily be lost. To avoid this, the intermediate lens is defocussed slightly so that the crystal of interest can be viewed within the diffraction spots and its position adjusted so that it does not move out of the field during tilting or rotation. After critical beam alignment, insertion of the objective aperture and stigmating of lenses, lattice images can be viewed at (2-5) x 10^6 times magnification on the fluorescent screen of the microscope. Images were recorded within 2 to 4 seconds.

3.4 Description of Specimen

The specimen used in this study is part of the same specimen used by Chen (1970) in her studies. The specimen is 68024 (pinkish white, Dungannon Township, Ontario). On the basis of chemical analysis, the following formula was reported by Chen, on the basis of Si + Al = 12.

68024 $(Na_{5.96}Ca_{1.51}K_{0.02})$ $(Al_{6.02}Si_{5.98}O_{23.90})$ $(CO_3)_{1.57}Cl_{0.06}\cdot 1.75H_2O$.

This analysis is similar to other $(Na,Ca)CO_3$ cancrinite analyses reported in the literature. A further discussion on the chemistry of cancrinite will be given in section 6.1.

CHAPTER 5

HRTEM RESULTS

4.1 Electron Diffraction Patterns of Cancrinite

Electron diffraction patterns showing various reciprocal-lattice sections of the cancrinite crystal were examined. Figure 4.1 shows a well-oriented electron diffraction pattern taken with the incident electron beam normal to the (001) plane. The circle drawn in the figure indicates the size and the position of the objective aperture used for taking the images in this study. The size corresponds to $\sim 0.42 \text{Å}^{-1}$ in reciprocal space (corresponding to a resolution ~ 2.4Å) and enables about 80 diffracted waves to contribute to imaging. Since (hko) reflections are permitted by the aperture, the resulting image is necessarily a two-dimensional structure image and it contains much more information than the one-dimensional lattice fringes obtained by using (00ℓ), (0k0) or (h00) reflections.

The a*-c* reciprocal-lattice planes are quite interesting as they show many important features. Figure 4.2 shows such a section in which the electron beam is parallel to the a-axis. The main lattice reflections ($a = 12.590$; $c = 5.117$Å) are quite strong compared to the non-Bragg reflections (superstructure reflections). Since cancrinite possesses a 2_1 screw axis, hkℓ reflections, where $h = k = 0$ and $\ell = 2n + 1$ are absent on X-ray precession photographs. These reflections whose intensities are less than the permissible reflections, are seen on electron diffraction patterns. These forbidden reflections can be explained as resulting from a very

Figure 4.1: Electron diffraction pattern of a cancrinite crystal taken with the incident beam normal to the (001) plane. The circle shows the size of the objective aperture used for imaging.

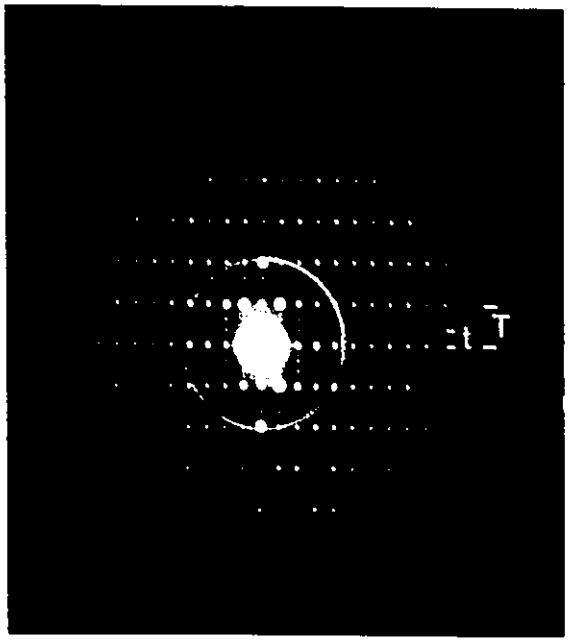

Figure 4.2: Electron diffraction pattern of a cancrinite crystal taken with the incident beam normal to the (100) plane. The circle shows the size of the objective aperture used for imaging. c* is vertical; a* is horizontal.

slight tilt of the crystal and thus a small deviation in the [100] axis orientation thereby permitting the forbidden reflections. These are enhanced by multiple diffraction when the crystal thickness is great (Iijima and Buseck, 1978). In fact, small changes in the orientation of a particular crystal, as detected by examination of the diffraction pattern, during study in the electron microscope are frequently observed, doubtless they are due to specimen heating, with consequent bending and stage drift. Alternatively, these extra reflections may be real, suggesting that the 2_1-screw axis is a pseudo axis. Similar observation was made by Barrer et al. (1970) using XRD.

Four sets of superstructures are seen in Figure 4.2. The two sets that lie closer to the main reflections are of lower intensity than the two sets that lie further away.

4.2 Characterization of Incommensurate Superstructures in Cancrinite

Superstructures are seen in diffraction patterns as satellites or superstructure reflections (non-Bragg reflections) in addition to the main reflections corresponding to the fundamental structure. The satellites usually divide the interval between the main reflections into simple integral parts, indicating that the unit cell of the superstructure is a simple multiple of that of the fundamental structure. However, studies on mineral phases, that is, decomposition or transformation from the high temperature forms to the low temperature forms show that complex superstructures are associated with such phase transformations (Sadanaga, et al. 1978). For these superstructures, only lower order satellites are observable, such as first, second and third order ones, and these satellites move continuously in reciprocal space, according to

composition and temperature, with no practical change in either intensity or position of the main reflections. In the case of these superstructures, the interval between the satellites and main reflection (t) cannot be expressed as a simple fraction of the interval between the main reflections (T). This character was emphasized by Sadanaga et al. (1978) on consideration of the periods of the supercells, expressed by N (= T/t). When N is integral, the structure is called integral or commensurate, otherwise, the structure is called non-integral or incommensurate. The electron diffraction pattern of cancrinite is shown in Fig. 4.2, where a* and c* represent the reciprocal axes. Along the c*-axis the repeat distance for the main reflections (= T in Fig. 4.2) is N times as large as the distance between the a*-axis and the nearest satellites (t). The N-values are non-integral such as 3.98 and 2.65, and are represented, as $3.98\underline{C}$[+] and $2.65\underline{C}$. The structure of cancrinite can therefore be represented as a supercell of the $N\underline{C}$ type with $a = \underline{A}$ and $c = N\underline{C}$ where $\underline{A}$ and $\underline{C}$ represent the translation vectors of the hexagonal type cell (c_o = 5.117Å and $1/a_o^*$ = 10.903Å). N-values and NC-values for various cancrinites are summarized in Table 4.1.

XRD studies reveal three or fewer sets of superstructure reflections for cancrinite from different localities (Table 4.1). However, Fig. 4.2 clearly shows four sets of superstructure reflections. It is interesting to note that Chen, 1970 XRD studies reveal only three sets of superstructures in spite of the fact that the same samples were used in both this and her studies. Furthermore, the distribution of the

---

[+] $\underline{C}$ is a vector quantity. From now on, underlined letters represents vectors whose scalar values will not be underlined.

Table 4.1 Summary of Values for Cancrinite Superstructure*

Sample No./ Locality	a_o (Å)	c_o (Å)	N_1	N_2	N_3	N_4	N_1C	N_2C	N_3C	N_4 C	Method/ Author
68024 Dungannon Tp.	12.62	5.13	4.0	2.65	1.58	--	20.5	13.6	8.1	--	XRD Chen, 1970
67002 Dungannon Tp.	12.62	5.13	3.47	2.80	1.54	--	17.8	14.4	7.9	--	XRD Chen, 1970
67001 Methuen Tp.	12.62	5.13	--	--	1.8	--	--	--	9.2	--	XRD Chen, 1970
69008 Methuen Tp.	12.61	5.12	--	--	1.79	--	--	--	9.2	--	XRD Chen, 1970
Litchfield, Maine, U.S.A.	12.75	5.14	--	2.33	--	--	--	12.0	--	--	XRD Jarchow, (1965)
Bancroft, Ont.	12.62	5.13	--	2.76	--	--	--	14.2	--	--	XRD Foit et al. (1973)
68024	12.590	5.117	3.98	2.65	1.61	1.34	20.37	13.56	8.24	6.86	EM, This study

*see text for explanation of symbols.

superstructure reflections (Fig. 4.2) is quite regular and higher orders of reflections are observable by EM than by XRD. In addition, as electron beams are diffracted by electrostatic potential fields of both the nucleus and orbital electrons, the intensity of the superstructure reflections for EM is greater than for XRD, where x-rays are diffracted only by the orbital electrons. This indicates a distinct advantage of EM over XRD in the studies of superstructure. Rinaldi and Wenk (1979) were able to observe diffuse satellites in the hkO diffraction patterns for franzinite first by electron diffraction and later confirmed by XRD using monochromatic Mo K_α radiation for strongly exposed precession photographs.

4.3 Electron Beam Damage of Cancrinite

A great deal of experimental difficulties were encountered in this study. These include the exact alignment of the crystal and problems of avoiding electron-induced radiation damage. These problems were also encountered by Iijima and Buseck, (1978), in their studies of stacking disorder in micas. Rate of electron beam damage was not reported by these authors. However, to overcome these difficulties, Iijima and Buseck resorted to one-dimensional lattice imaging, obtainable from thicker samples and requiring neither exact alignment of the crystal nor high magnification for recording the images. It is not surprising, in view of the above difficulties, that no HRTEM work has been published on cancrinite (Buseck, personal communication).

Electron-induced radiation damage is particularly severe for the a*-c* section. This is clearly seen on examination of the diffraction patterns obtained from such a section (diffraction patterns are recorded

in 10 to 15 seconds after critical orientation of the crystal). Figures 4.3a-4.3e show increase in radiation damages to various extent. Figure 4.3a is typical of an undamaged crystal. Figure 4.3b shows the more intense sets of superstructure reflections with the less intense sets completely disappeared. Figures 4.3c and 4.3d are deliberately over-exposed with Figure 4.3c showing the superstructure reflections as diffuse streak parallel to a* but individual spots are still recognizable, while with increasing damage the spots are no longer spots but diffuse streak (Fig. 4.3d) until they completely disappear (Fig. 4.3e). Essentially the same results were obtained by thermogravimetric and x-ray diffraction analyses of heated crystals (Chen, 1970; Foit et al., 1973). These authors interpreted their observations as due to a loss of volatiles, in particular H_2O and CO_2 and concluded that these volatiles are the major contributors to the formation of the superstructure reflections.

In terms of radiation damage seen in the images, the thinner the crystal the more severe is the radiation damage. However, there is a marked difference in radiation damage experienced by the sections normal to the c-axis and that of the a-axis. For the (001) plane, damages begin at the thin edge and progress to thicker regions. In the (100) plane, damage begins randomly at discreet centres and spread outward as elipses with the long-axes approximately parallel to $[210]$, indicating a place of structural or chemical weakness perpendicular to c. This, may be the basal cleavage (001) of cancrinite which, however, is poor compared to (100) cleavage which is perfect.

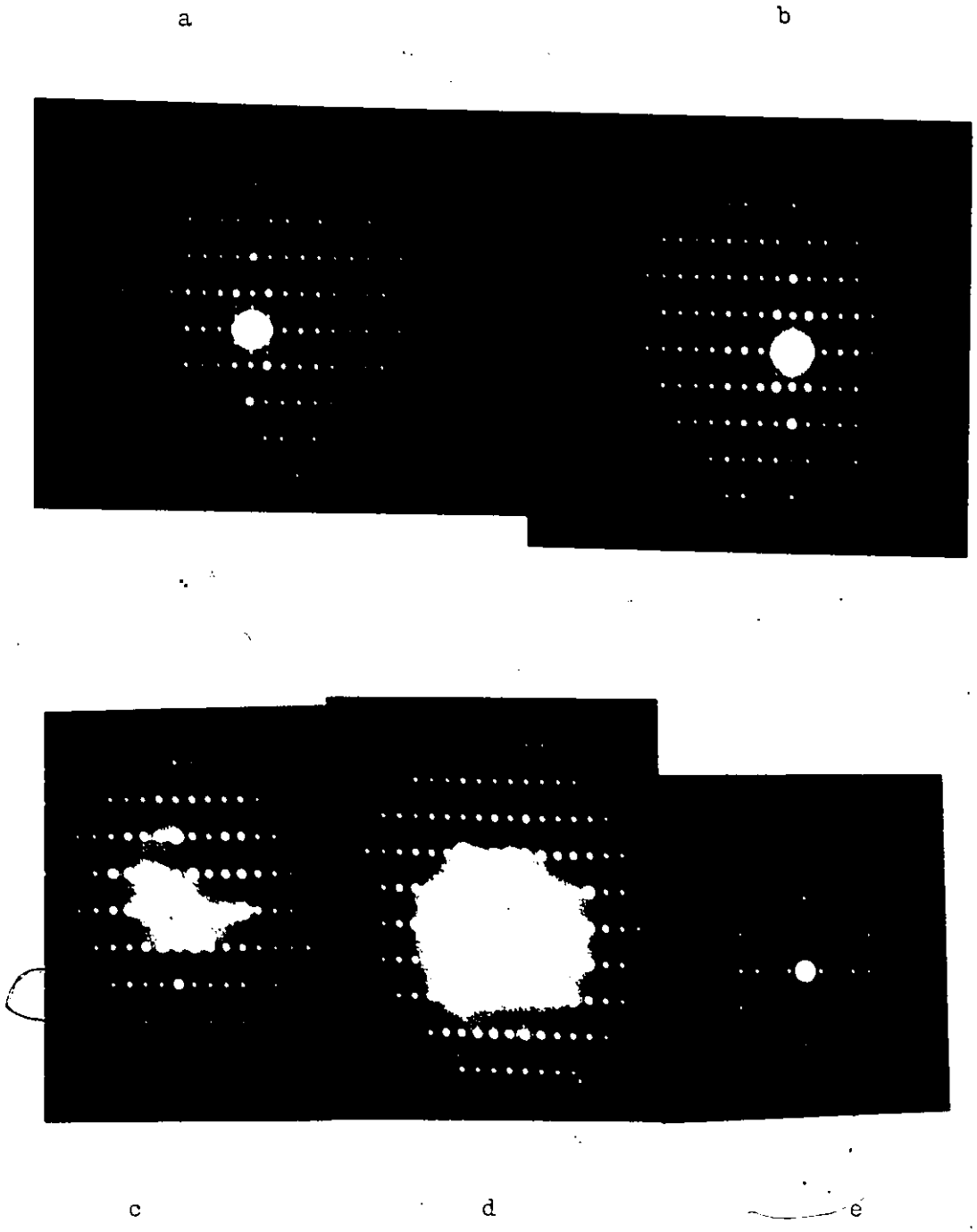

Figure 4.3: Diffraction patterns showing the effect of increasing radiation damage to the (100) reciprocal-lattice plane. (a) is typical of an undamaged crystal; (b) superstructure reflections of the less intense sets completely disappear and only the strong sets of reflections are seen; (c) superstructure reflections are seen as diffuse streak with individual spots still recognizable while in (d) only faint streaks are seen until they completely disappear in (e). (c) and (d) are deliberately overexposed to show the faint streaks. a* is horizontal; c* is vertical.

4.4 Calculated Images of Cancrinite

It is necessary to compute images which are comparable to images obtained experimentally since this leads to unambiguous interpretation of structure images. However, in the past, it was a common practice to obtain a defocus series of images experimentally. This series commonly include an image at the optimum defocus conditions. Computations were then made to reproduce the defocus series of images obtained experimentally, rather than reproduce any one given experimental image. This serves as a check on the computation accuracy to reproduce images obtained experimentally, which was questionable.

It was not possible to obtain a defocus series experimentally for cancrinite due to the severe radiation damage it suffers in the electron beam. However, as the accuracy of the computed images have increased considerably in recent times, it is no longer necessary to obtain a defocus series experimentally. Instead, images are computed for various operating conditions until a match can be made with an image obtained experimentally. Having obtained such a match, the defocus series can then be reproduced by computations (O'Keefe et al. 1978). All of this, of course, assumes that the crystal structure is known.

Calculated images of cancrinite (based upon site occupancies as determined by Jarchow, 1965) are shown in Figures 4.4 and 4.5 which correspond to the a-axis projection and the c-axis projection respectively.

(a) Calculated images for a-axis projection

The calculation simulated the inclusion of 19 diffraction beams within the objective aperture (centred about the incident beam). The series of images calculated at thickness ranging from 12.75 to 102.0Å

at values of defocus ranging from +600 to -1500Å are shown in Figure 4.4. The range of general image interpretation in terms of the crystal structure is given in Table 4.2.

Table 4.2: Range of image interpretation in terms of the crystal structure (a-axis projection)

Thickness (Å)	Defocus Å
12.75	-200 to -1100
25.5	-200 to -1100
51.0	-200 to -1100
76.5	-100 to -1100
102.0	-100 to -1000

The photographs of the images are not very good as regions appearing white in fact show some contrast. In terms of the crystal structure, the best region is for defocus values ranging from -700 to -1000Å. There is overall gradual variation in contrast for some individual image. This is due to lineprinter faults and also slight tilt in the camera when taking the pictures.

The images in Figure 4.4 are oriented such that the c-axis is across the page and the a*-direction is vertical. A unit cell can easily be recognized by comparison with the structural plan shown in Figure 1.2.

(b) Calculated images for c-axis projection.

The calculation simulated the inclusion of 55 diffracted beams within the objective aperture (centred about the incident beam).

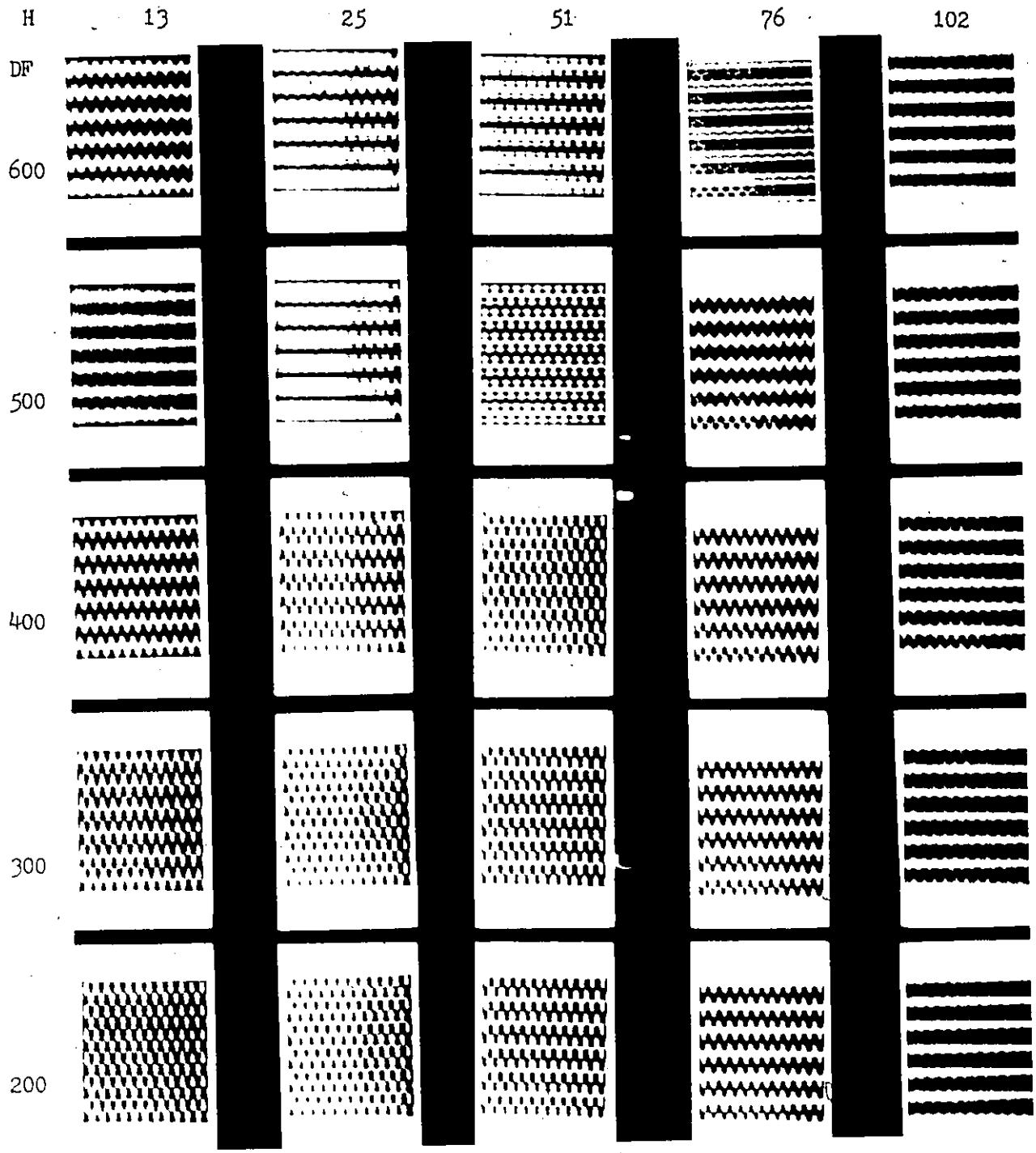

Figure 4.4: Computed images of cancrinite projected down the a-axis at thicknesses (H) from 12.75 to 102.0Å and at defocus values (DF) from 600 to -1500Å. Note that there is no appreciable change in contrast within the thickness range investigated for the (100) section. The range of image interpretation in terms of the crystal structure is given in Table 4.2.

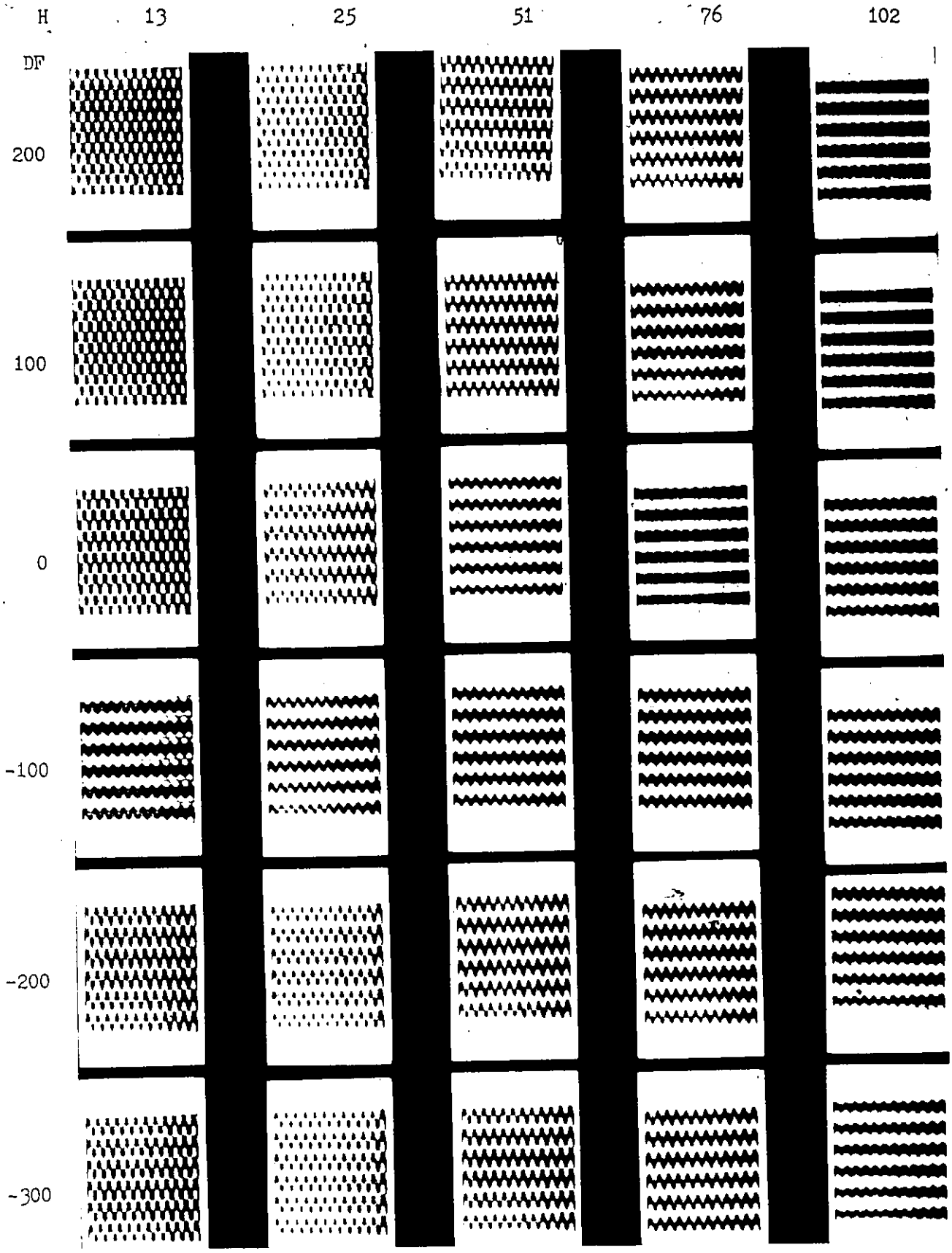

Fig. 4.4 (cont'd.)

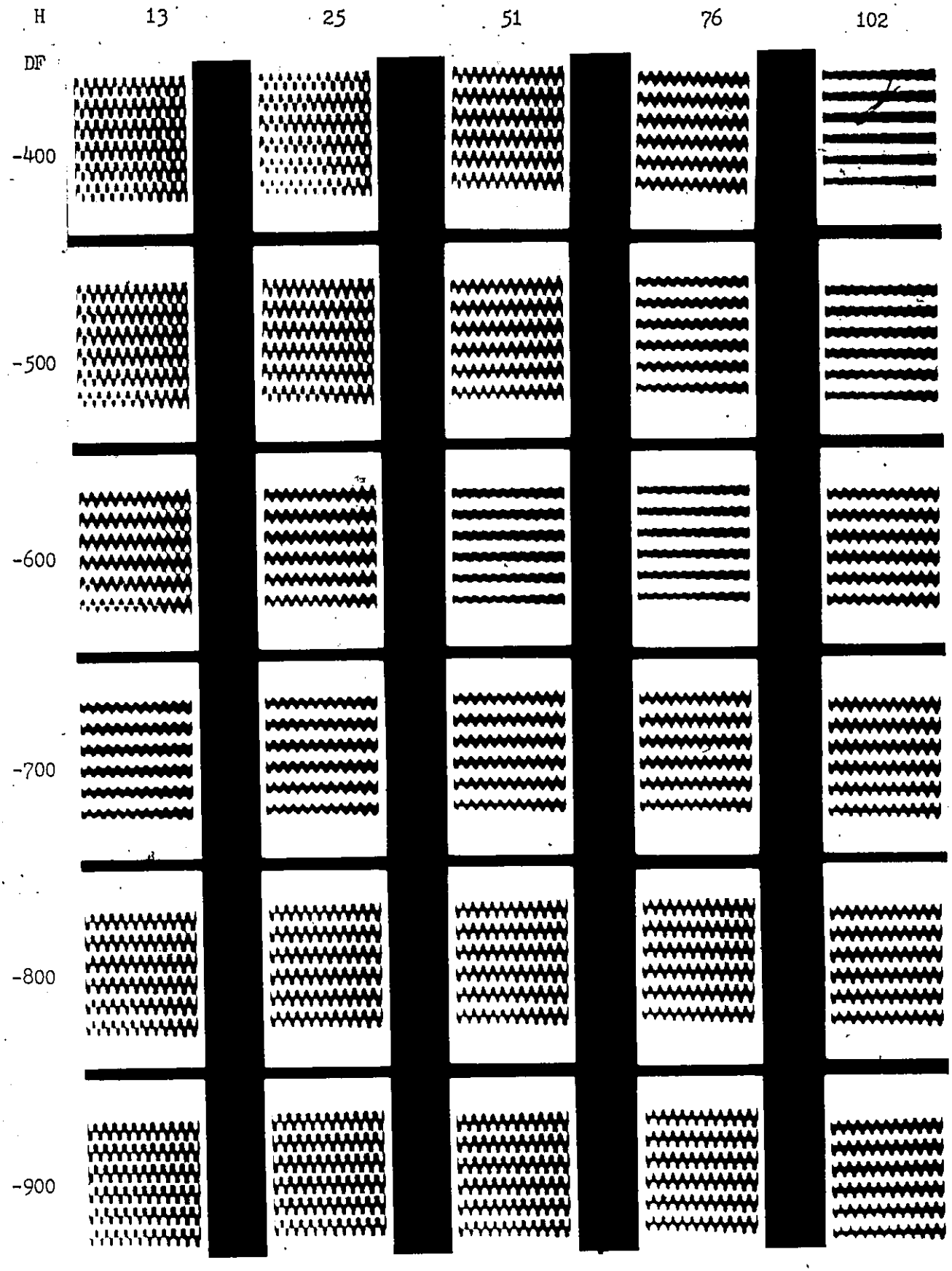

Fig. 4.4 (cont'd.)

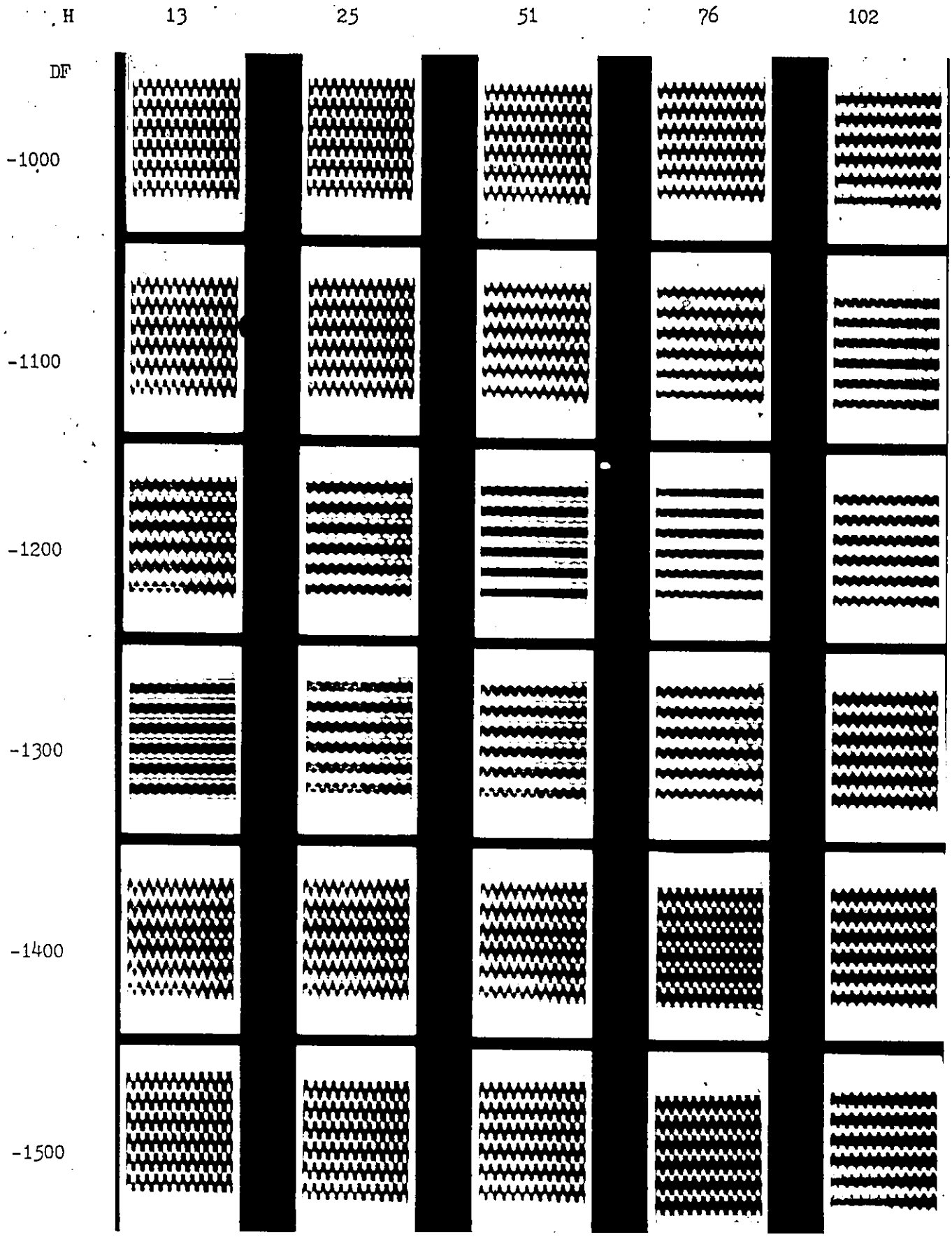

Fig. 4.4 (cont'd.)

The slice thickness was limited to 5.14Å and calculations were made for gradually increasing crystal thickness to a maximum value of 102.8Å. Defect of defocus was sampled at intervals of 100Å in the region from +600 to -1500Å for the c-axis projection.

Figure 4.5 shows that there are marked changes in image contrast as physical parameters (thickness and defocus) change. The images can be interpreted, in terms of the crystal structure, within the range given in Table 4.3.

Table 4.3: Range of image interpretation in terms of the crystal structure (c-axis projection)

Thickness (Å)	Defocus (Å)
5.14	-400 to -1100
25.7	-400 to -1100
51.4	-200 to -1000
77.1	0 to -800
102.8	+400 to 0

Within this range, a unit cell can easily be identified if the image is compared to the structural plan shown in Fgiure 1.1.

Table 4.3 shows that the range of crystal structure interpretation shifts to higher (more positive) defocus values as the crystal thickness increases. Parallel to this trend is continuous change in contrast and eventually there is complete reversal of contrast. This is clearly seen by comparing the "ideal" image (H = 51Å; DF = -900Å) with image (H = 103Å; DF = +200Å). The former, shows the large 6_3 channels having light contrast and the trigonal channels having heavy contrast while the latter shows the exact opposite.

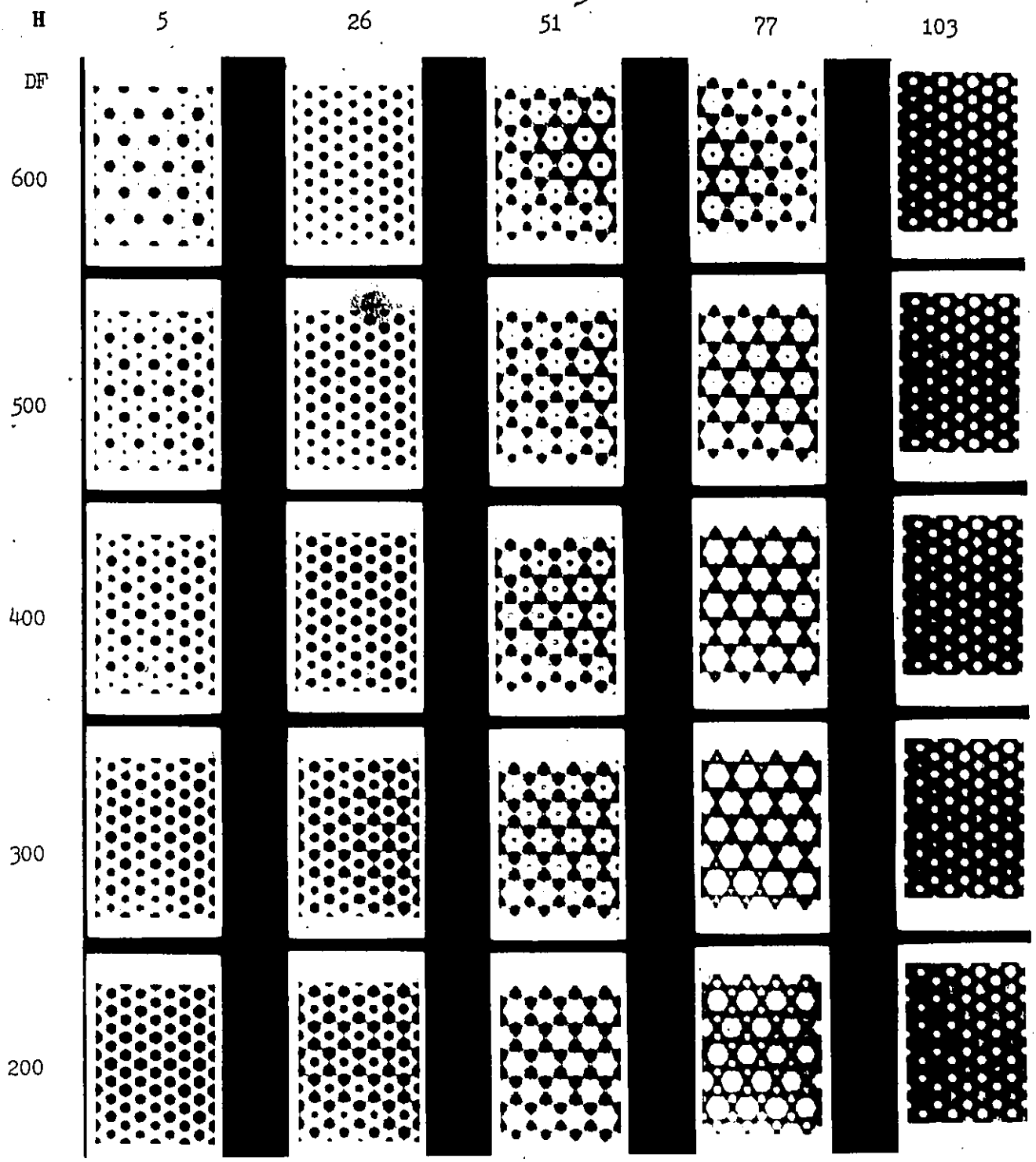

Figure 4.5: Computed images of cancrinite projected down the c-axis at thicknesses (H) from 5.14 to 102.8Å and at defocus values (DF) from 600 to -1500Å. Note how the region of interpretable image contrast shifts to higher defocus values as crystal thickness increases. The range of image interpretation in terms of the crystal structure is given in Table 4.3.

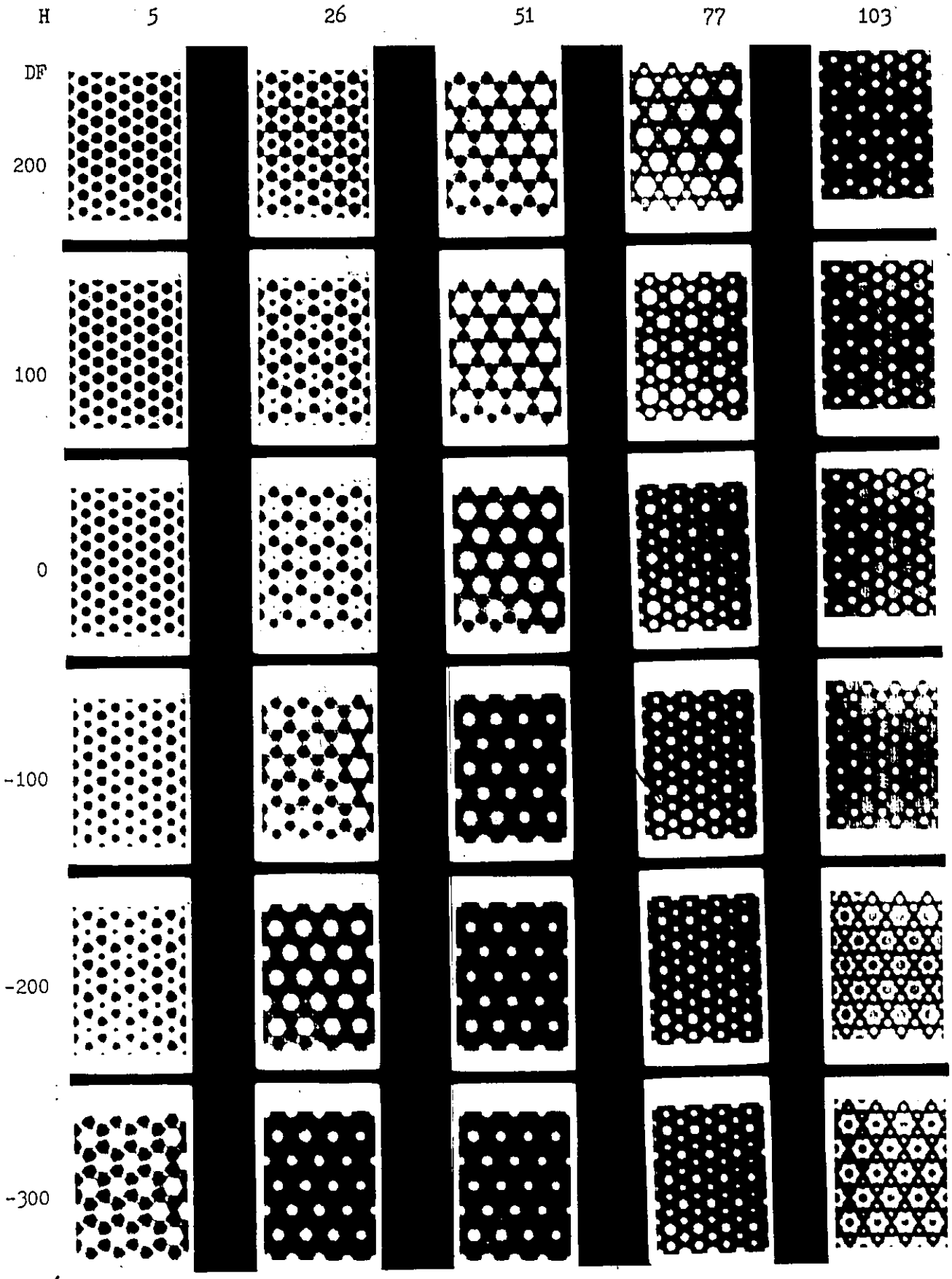

Fig. 4.5 (cont'd.)

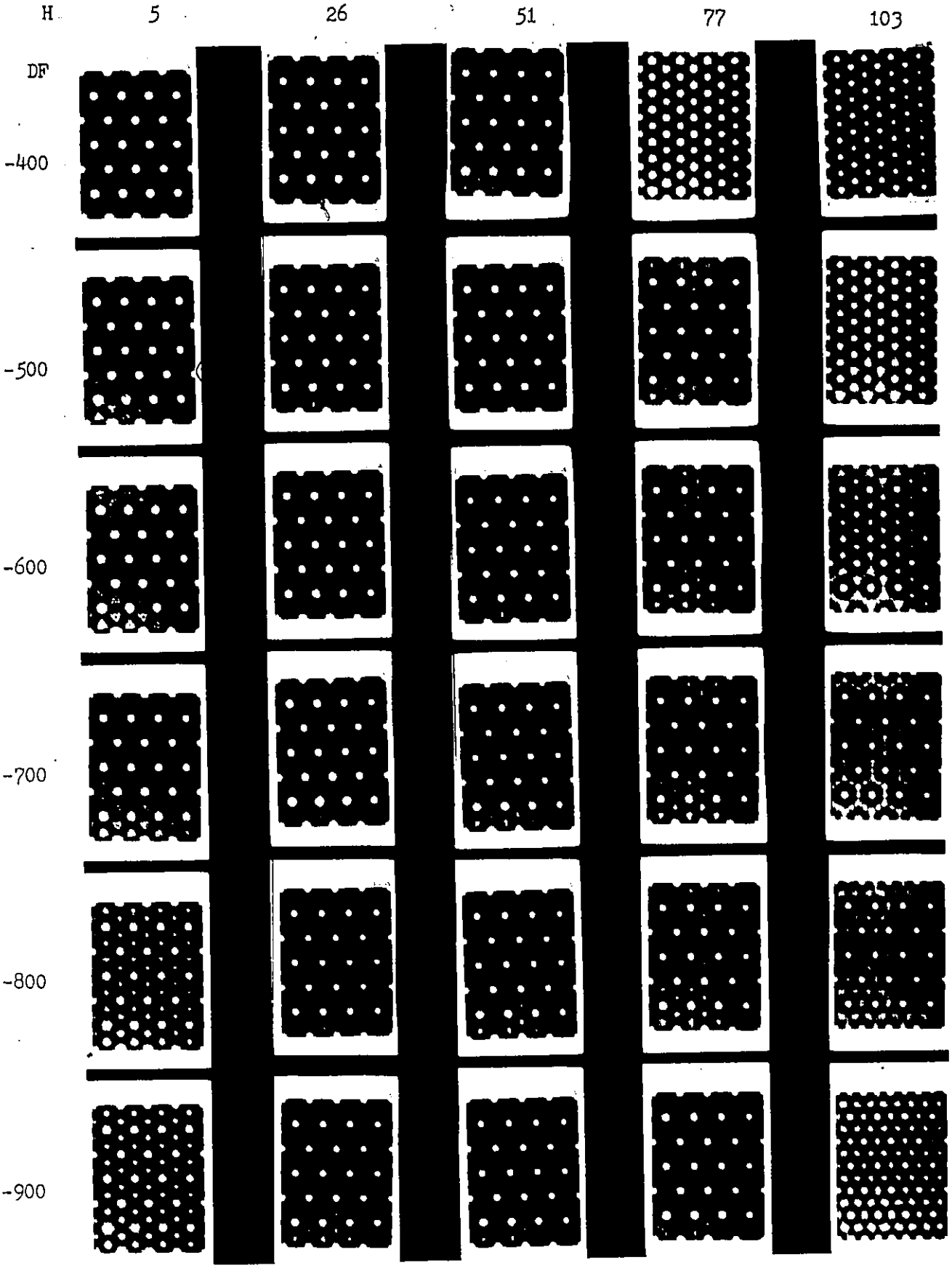

Fig. 4.5 (cont'd.)

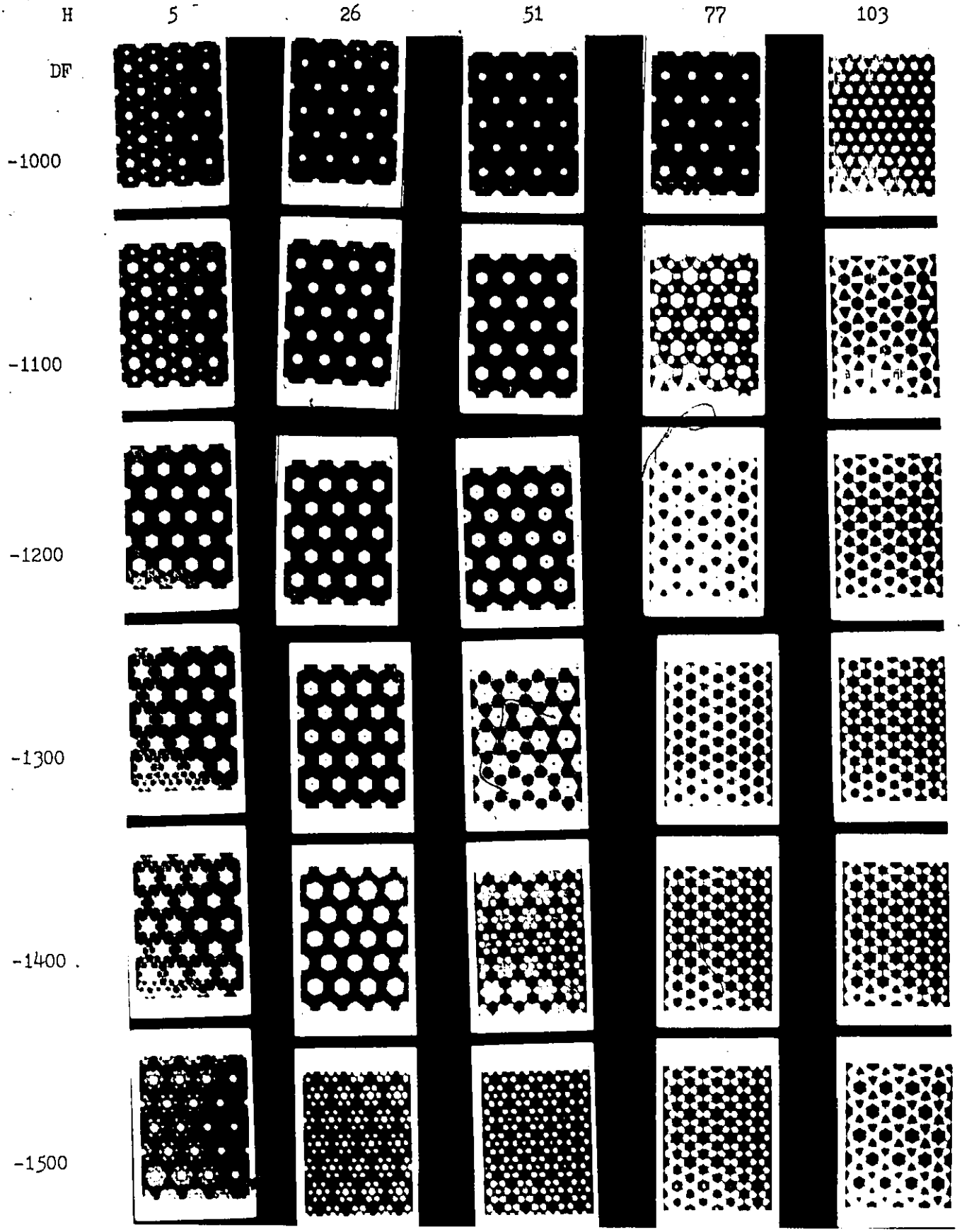

Fig. 4.5 (cont'd.)

4.5 Matching of crystal structure, experimental and calculated images

An intuitive interpretation of contrast in the experimentally observed images is possible since it has been shown experimentally and theoretically (Skarnulis, Iijima and Cowley, 1976), that light contrast is produced by regions of low electrostatic potential (eg. light atoms and empty channels), while heavy contrast is produced by regions of high electrostatic potential (eg. heavy atoms, columns of heavy atoms or dense rows). If the projected distances between the heavy atoms are sufficiently large compared with the resolution of the microscope (~3Å in the instrument used in this study), they are imaged as separate dots; otherwise they are smeared into large blobs. In the case of cancrinite, contrast in the electron image is developed between the channels and the surrounding framework atoms.

(a) A-axis projection of Cancrinite

In spite of the difficulties encountered in recording images of the a-axis projection of cancrinite, an excellent image is shown in Figure 4.6, which corresponds to the (0kℓ) electron diffraction pattern shown in Figure 4.2. A unit cell is outlined in Figure 4.6 (c = 5.117Å; $1/a^* = 10.903$Å) and its size serves to indicate the magnification. This image should be compared with the structural plan shown in Figure 1.2, as there is a direct correspondence between the two. This image is quite interesting as it gives the general contrast expected when considering the structural plan. From the structural plan, one would expect to resolve the double set of 6-member rings (free diameter ~4.5Å) that are

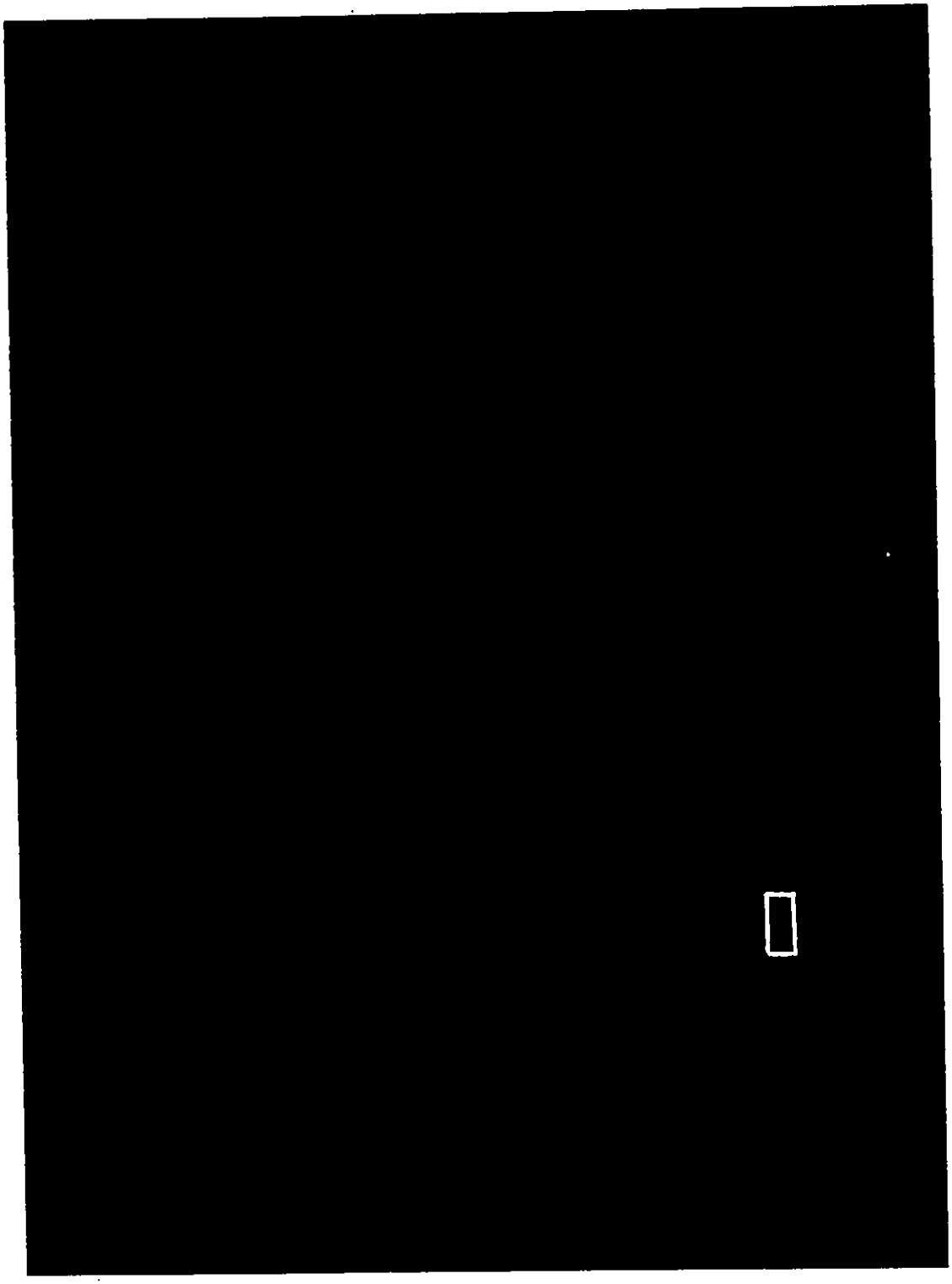

Figure 4.6: Bright-field high-resolution structure image of cancrinite (68024) taken near the optimum defocus of about -900Å, with the electron beam normal to the (001) plane. The unit cell outlined ($c = 5.12$, $1/a^* = 10.90$) serves to indicate the magnification.

parallel to the c-axis. These sets of rings would be expected to show light contrast and be separated by the four-member rings (free diameter ~3Å) that are expected to show heavy contrast, as these rings are small and cannot be resolved at the resolution obtainable from the microscope used.

Figure 4.6 shows small distinct rows of spots parallel to the c-axis. These spots are approximately of the same sizes and their geometry conforms to that expected from consideration of the structural plan and calculated images (eg. H + 51Å; DF = -900Å, Fig. 4.4). It should be pointed out that images of the a* - c* sections are quite regular, that is, they do not show any unusual features such as stacking faults, which was believed by Rinaldi & Wenk (1979) to be common in cancrinite and were responsible for its superstructure.

(b) C-axis projection of cancrinite

A good example of one of the best experimentally observed images is shown in Figure 4.7, which corresponds to the electron diffraction pattern shown in Fig. 4.1. In Figure 4.7, a unit cell is outlined and its size (a = 12.59Å) serves to indicate the magnification. Matching can generally be made among the observed image, computed image and the structural plan if the variation in contrast seen in the observed image is ignored for the moment. From the structural plan (Fig. 1.1) one would expect the two types of channels to have about equal intensity since the trigonal channels (diameter ~5.2Å) are presumably filled with two Na(Ca) and two H_2O per channel per cell while the 6_3 channels (diameter ~8.7) are presumably filled with 5 Na(Ca) and 1.5 CO_3 per channel per cell, which results in about equal electron density per unit

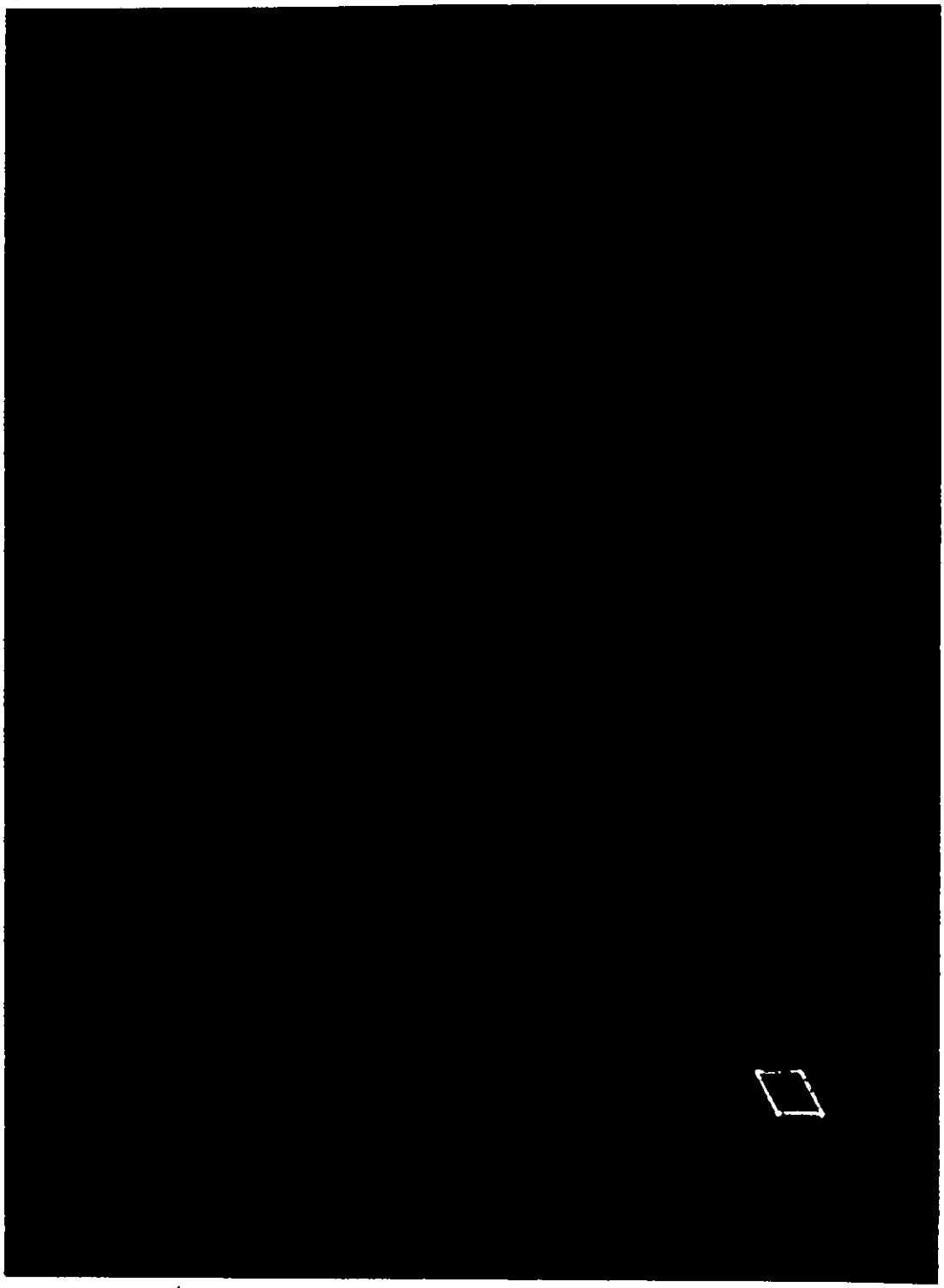

Figure 4.7: Bright-field high-resolution structure image of cancrinite (68024) taken near the optimum defocus of about -900Å with the electron beam normal to the (001) plane. The unit cell outlined (a = 12.59Å) serves to indicate the magnification.

area. Both channels appear light since the contrast is developed between the channels and the surrounding framework atoms. This prediction is confirmed by the computed imaged (eg. H = 51; DF = 900Å, Fig. 4.5). The computed images show the large 6_3 channels to have lighter contrast than the trigonal channels which is due to the photographer not being able to reproduce low intensity in these large channels.

The experimental image shown in Figure 4.7 show little variation in contrast among the trigonal channels. However, there is definite variation in contrast among the large 6_3 channels in a near-random manner. Furthermore, the large 6_3 channels show heavier contrast than the trigonal channels. This would suggest that all the Ca is in the 6_3 channels, in opposition to Jarchow's model, in which Ca is statistically distributed with Na in the cages. Except for the variation in contrast of the 6_3 channels, the experimental image corresponds to the computed image (H = 51Å; DF = -900Å).

The above observations allow one to make the following general statements: (1) the trigonal channels are quite ordered in terms of the chemical constituents it contains since there is no appreciable variation in contrast for these types of channels. (2) The light contrast seen in the trigonal channels suggest that they do not contain Ca, which consists of twice as much electron density as Na. Consequently, these channels are filled by Na while the Ca is restricted to the large 6_3 channels. (3) The dark 6_3 channel regions variation in intensity in a near-random manner indicates the variability of the proportions of Ca, Na and CO_3 in the lines of atoms projected in these sites, with little tendency for ordering. Similar variation in contrast observed in HRTEM

study of tourmaline crystals were interpreted in a similar way (Iijima et al. 1973).

Since stacking faults were believed to be common in cancrinite (Rinaldi & Wenk, 1969), and as none were observed in this study, it is interesting to consider what stacking faults would look like in electron micrographs for cancrinite-related minerals. Plate 1, taken directly from Rinaldi and Wenk (1979) shows electron diffraction patterns of liottite, afghanite and franzinite and their corresponding electron images at low resolution. It should be noted that no obvious superstructure reflections of the cancrinite type are observed in these minerals. Even though stacking faults are demonstrated, they are not common on a few unit cell scale. These observations will be re-examined in the final chapter, in view of a model for the superstructures in cancrinite.

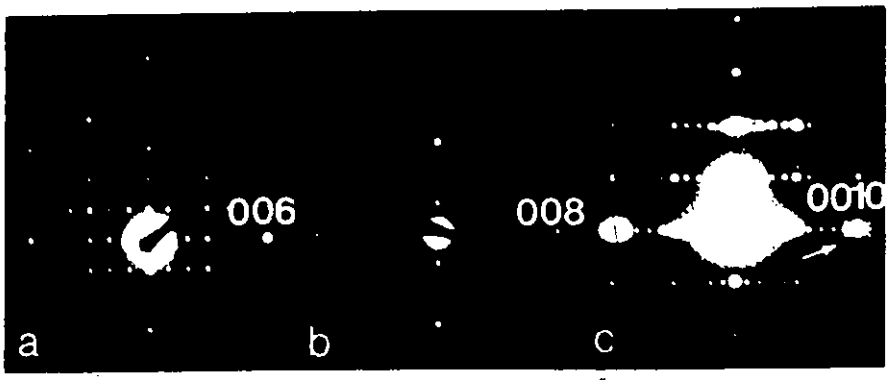

Fig. 2. Electron diffraction patterns of (*a*) hottite, (*b*) afghanite, and (*c*) franzinite. c^* is horizontal. Notice the correspondence of reflections 006 in (*a*) with 008 in (*b*) and 0,0,10 in (*c*) which denote the basic 2·6 Å stacking unit. Satellites about 0,0,10 in (*c*) (arrow) are probably due to short range Al, Si order.

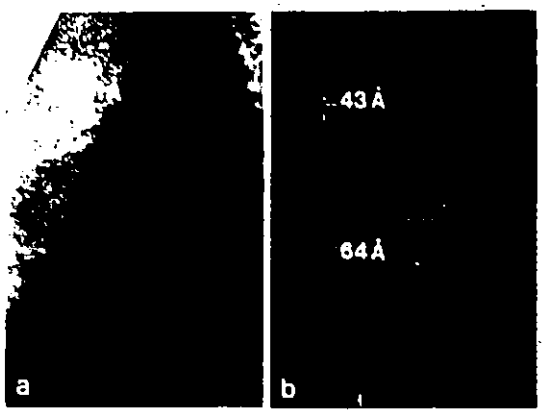

Fig. 3. 00*l* fringes in afghanite, imaged in dark field. (*a*) Region with regular 21·3 Å fringes. (*b*) Local area with 2× and 3× 21·3 Å fringes due to periodic stacking. The two stacking sequences occur next to each other in the same crystal as (*a*).

PLATE 1

Taken from Rinaldi and Wenk (1979)

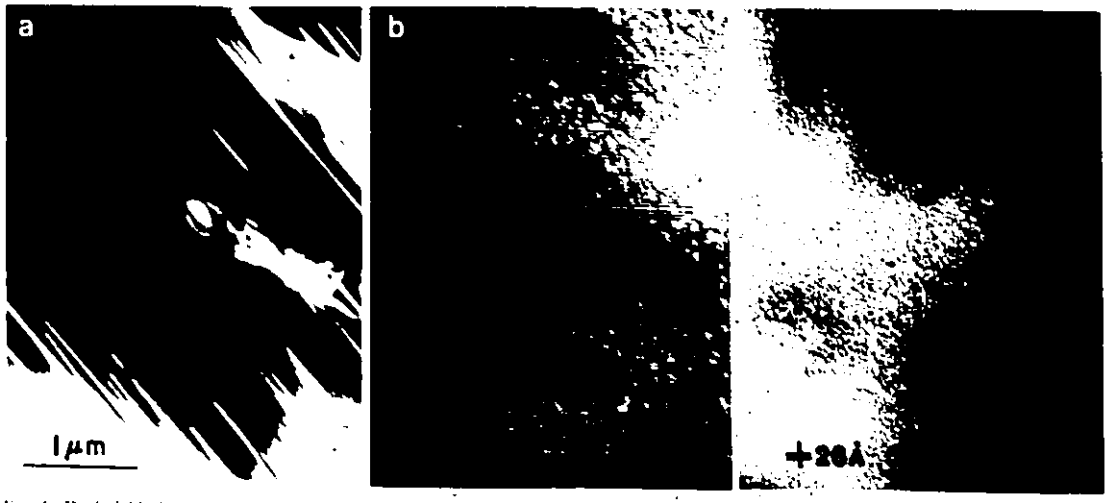

Fig. 4. Dark field photomicrographs of franzinite: (*a*) displays stacking faults imaged at low magnification; (*b*) at higher resolution. In (*b*) we see numerous faults which interrupt the regular 26 Å stacking with insertion of smaller and larger units; (*c*) is taken at the same magnification as (*b*) but of a part of the crystal which is unfaulted.

CHAPTER 5

XRD RESULTS

On the basis of the HRTEM results, it seems possible to re refine the crystal structure of cancrinite using X-ray diffraction methods. Calcium is a stronger scatterer than sodium, thus structural investigation could be successful in determining whether the Ca is in the large channels or in the cages. Also, the abundance of carbonate ion with its high point symmetry and the fact that the group as a whole is a reasonable scatterer of x-rays, should help define positional disorder of this in the structure.

5.1 X-Ray Refinement for $(Na,Ca)CO_3$ Cancrinite

The standard procedures for collecting X-ray data, reduction of data and final refinement are described in detail elsewhere (Buerger, 1960; Hawthorne, 1973). The computer programs for data processing and refinement were from X-Ray 78, Program System for X-Ray Crystallography, compiled by J. M. Stewart, University of Maryland, adapted by H. D. Grundy for the CYBER 730. The X-ray system at McMaster University is described at length by Hawthorne (1973).

Initial parameters for least-squares refinement were the final parameters of the structure as determined by Jarchow (1965). At a very early stage in the refinement, the population parameter for Ca (in cages) suggest that there were too much electron density in the cages. Thus, following the electron microscope observations, all the calcium were

placed in the large channels and two sodiums were placed in the cages. The population parameters were refined for Na(1), Na(2) and CO_3, and they were fixed at the values shown in Table 5.1 for the remaining structure refinement. The refined parameters for Na(6.0), C(1.52) and Ca(1.53) agrees well with the chemical analysis (Table 6.1).

The residual R-factor ($R = \sum(|F_o| - |F_c|)/\sum|F_o|$) is quite low ($R = 0.029$) and thus indicates a well refined structure for cancrinite. Final atomic coordinates and isotropic temperature factors are given in Table 5.1. Anisotropic temperature factor coefficients of the form

$$\exp -\{\sum_{i=1}^{3}\sum_{j=1}^{3} h_i h_j \beta_{ij}\}$$

are given in Table 5.2.

Anisotropic temperature factors are difficult to compare directly as they have both magnitude and direction (tensors). However, the isotropic temperature factors have only magnitude and can be compared directly. Generally, the framework atoms together with $Na_2(Ca)$ are well defined, both thermally and positionally in agreement with previous observations of complete Al-Si order in cancrinite.

Initially, oxygen of H_2O (O(6)) had a large temperature factor which indicates positional disorder and following Jarchow (1965), the water molecules were statistically distributed over three similar sites close to the three-fold axes. This immediately leads to a reduction in the temperature factor. Studies on the proton of H_2O in cancrinite by the PMR method (Sokolov et al., 1977) suggest that there are hydrogen bonding between the H_2O molecules and pairs of O(2) anions of the alumino-silicate framework. There are three possible O(2) anions pairs

Table 5.1 Parameters of (Na,Ca) CO_3 Cancrinite (estimated standard deviations in parenthesis).

Atom	Position Based on $P6_3$	Fractional Occupancy	X	Y	Z	Isotropic Temperature factor B($Å^2$) x 10^2
Al	6	1.00	0.0752(1)	0.4125(1)	0.7510(3)	0.758
Si	6	1.00	0.3277(1)	0.4103(1)	0.7500(0)	0.695
O(1)	6	1.00	0.2027(2)	0.4043(2)	0.6574(5)	1.471
O(2)	6	1.00	0.1131(2)	0.5635(2)	0.7281(7)	2.016
O(3)	6	1.00	0.0295(2)	0.3487(2)	0.0610(5)	1.448
O(4)	6	1.00	0.3131(2)	0.3566(2)	0.0439(5)	1.581
O(6)	2	0.33	0.6233(12)	0.3239(42)	0.6873(26)	7.661
O(51)		0.38	0.0572(8)	0.1163(8)	0.6728(23)	3.532
O(52)		0.38	0.0587(8)	0.1194(8)	0.9137(29)	4.322
C1		0.38	0.0000	0.0000	0.6728	3.317
C2		0.38	0.0000	0.0000	0.9137	5.330
Na(1)	2	1.00	0.6666	0.3333	0.1339(11)	4.908
Na_2(Ca)	6	1.13	0.1232(1)	0.2490(1)	0.2959(3)	1.878

Table 5.2 Anisotropic Temperature factor Coefficients for $(Na,Ca)CO_3$ Cancrinite (estimated Standard Deviations in Parenthesis).

Atom	β_{11}	β_{22}	β_{33}	β_{12}	β_{13}	β_{23}
Al	0.00713(30)	0.00862(31)	0.00699(32)	0.00429(27)	0.00005(39)	0.00066(42)
Si	0.00650(27)	0.00779(27)	0.00656(28)	0.00389(22)	0.00020(36)	0.00026(36)
O(1)	0.01133(92)	0.02186(103)	0.01093(86)	0.01122(86)	0.00055(82)	0.00170(89)
O(2)	0.02207(98)	0.01152(85)	0.02689(137)	0.01135(77)	0.00134(124)	0.00120(115)
O(3)	0.01156(92)	0.02200(106)	0.00988(111)	0.00919(85)	0.00350(79)	0.00457(90)
O(4)	0.01593(98)	0.02244(111)	0.00906(106)	0.01327(92)	0.00132(85)	0.00447(89)
O(51)	0.01229(320)	0.01246(313)	0.08122(755)	0.00555(269)	0.00002(348)	0.0043(353)
O(52)	0.01472(391)	0.01477(351)	0.10017(968)	0.00860(325)	0.00063(473)	-0.00849(471)
O(6)	0.08881(1049)	0.10824(1397)	0.03278(619)	0.06979(1669)	0.003532(552)	-0.00554(977)
C(1)	0.02018	0.02018	0.05915(961)	0.01009(315)	0.00000	0.00000
C(2)	0.01059	0.01059	0.13873(3229)	0.00529(182)	0.0000	0.0000
Na(1)	0.03117	0.03117	0.08491(346)	0.01559(49)	0.00000	0.0000
$Na_2(Ca)$	0.01139(46)	0.01790(52)	0.02705(80)	0.00938(42)	-0.00183(50)	-0.00125(52)

and hydrogen bonds are statistically formed to each pair. The two-fold axis of the water molecule is approximately parallel to the 6_3 axis. The O(6)-O(2) distance (~3Å) suggest that the hydrogen bonds are fairly weak (Brown, 1976).

Since H_2O is positionally disordered and Na(1) forms one of its bond to H_2O, it is expected that Na(1) should disorder in a manner similar to H_2O. Furthermore, the large temperature factor for Na(1) would suggest some disorder.

The position of the carbonate group at the initial stage of the refinement were those of Jarchow (1965). This resulted in a rather large temperature factor for the atoms of the CO_3 group which strongly suggested positional disorder. Difference Fourier maps were calculated with carbon removed from the structure model. Figure 5.1 shows a difference Fourier section through the carbon sites. The maximum density is clearly seen in four places. This shows that there are two non-equivalent crystallographic sites for carbon (C(1) and C(2)). These positions were then used in the refinement and there was a drastic decrease in the temperature factor. However, it is still fairly large suggesting large thermal motion together with possible disorder along the c-axis. The thermal ellipsoids of the atoms of the CO_3 group have their long-axes parallel to the c-axis which is also the orientation of the ellipsoid for Na(1) (Fig. 5.2). This would suggest that there is chemical communication between the large channels via the Na(1) in the cages. Therefore, the large channels are not independent of each other.

In terms of the coordination sphere for $Na_2(Ca)$, either of the non-equivalent sites are equally good for coordination to $Na_2(Ca)$. This

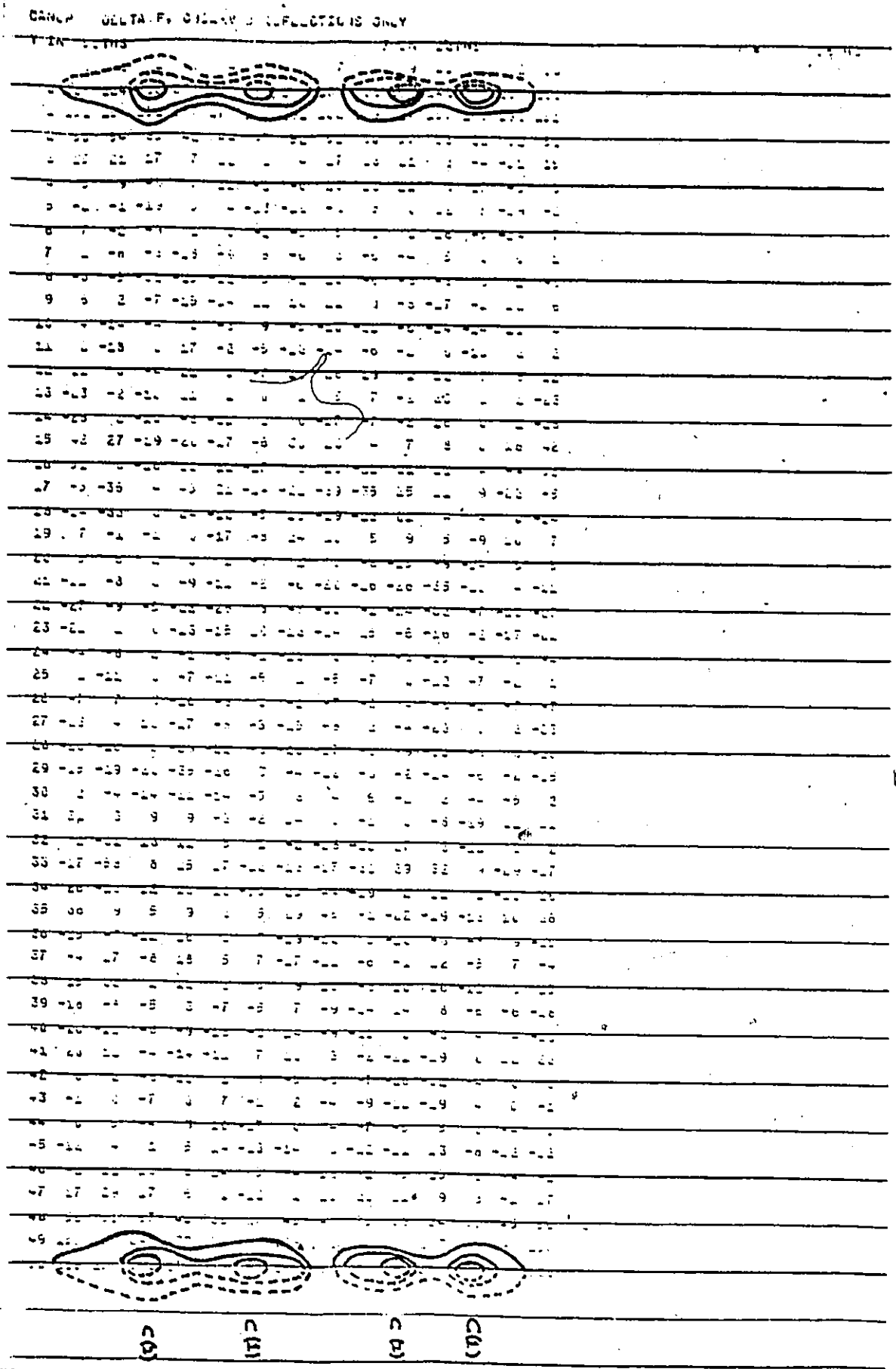

Figure 5.1: Difference fourier section through the carbon-sites, calculated with the carbons removed from the structure model.

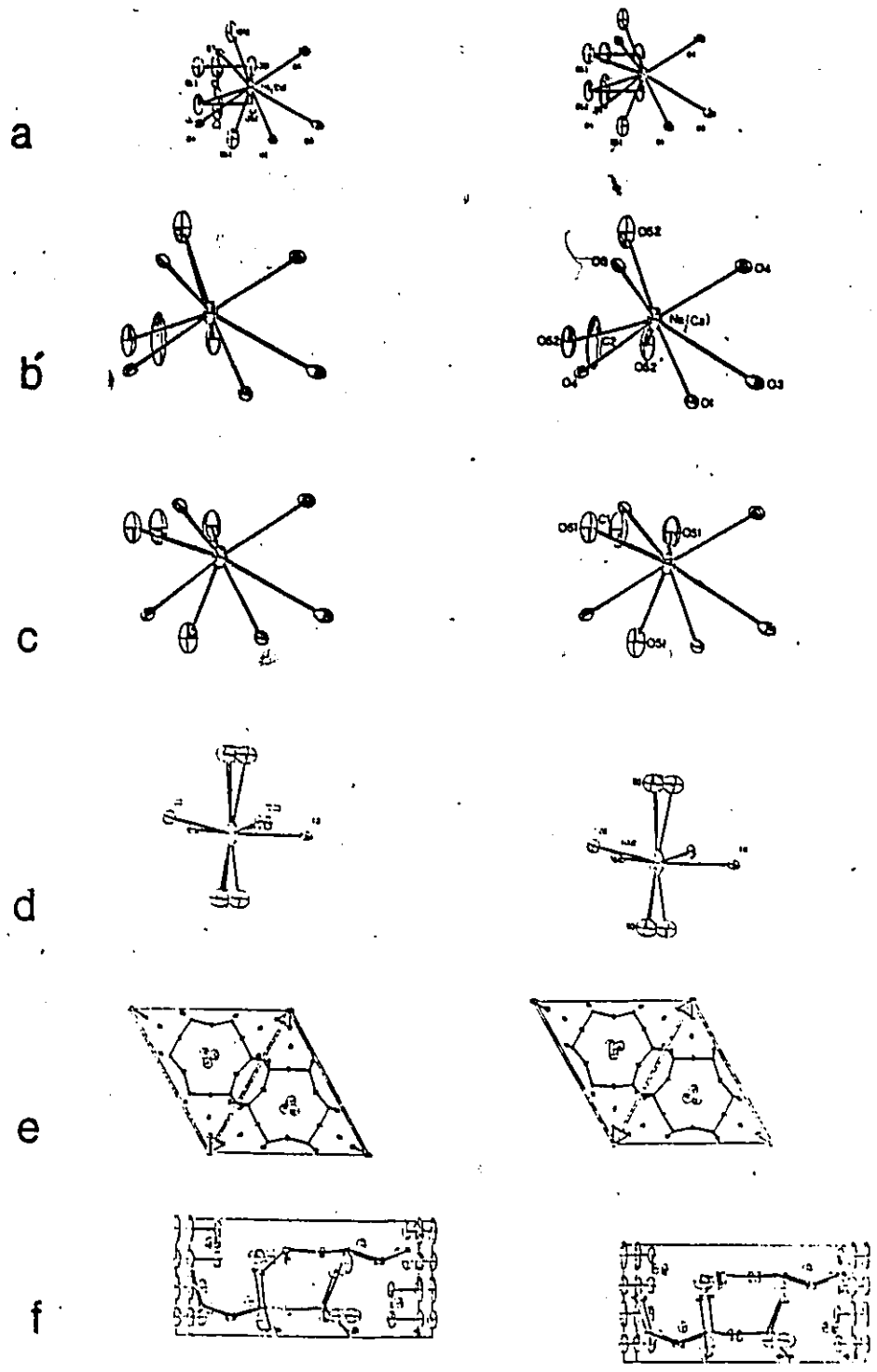

Figure 5.2: Stereoscopic pairs of cations environment (a - d) and also of the unit cell view down the c-axis (e) and down the a-axis (f).

is clearly seen in the stereoscopic pairs shown in Figures 5.2. In Figure 5.2a both environment are shown together while Figure 5.2b and Figure 5.2c show each environment separately. These stereoscopic pairs are seen looking down the a-axis.

The chemical environment of sodium (Na(1)) within the cage is shown in stereoscopic pairs looking down the a-axis, (Fig. 5.2d) and finally, Figure 5.2e and Figure 5.2f show a unit cell in stereoscope as seen looking down the c- and a-axis respectively.

5.2 Bond Valence Analysis

Calculations were made on bond-strengths using the model of Brown and Shannon (1973). The bond lengths are transformed into bond valences which have the property that the sums of the valences around each atom equal the atomic valence. Two different sets of curves ('a' = "individual" curves; 'b' = universal curves (Brown and Shannon, 1973)) were used and the results are given in Table 5.3.

The curves of sets 'a' give better results than curve 'b' for both Al and Si and bond strengths values are very close to that expected.

The two similar environments for $Na_2(Ca)$ have comparable bond strengths values for similar sets of curves. However, curves for set 'a' have values closer to that expected (1.13). The coordination for $Na_2(Ca)$ is 8-fold but the coordination sphere is distorted (Fig. 5.2).

The bond strength values around Na(1) calculated from both sets of curves are close to 1.0 but set 'a' tend to give a slightly better value. The coordination for Na(1) is 8-fold and its coordination sphere is more regular than $Na_2(Ca)$, but the bond to the H_2O above Na(1) is shorter than the bond to the H_2O below it.

Table 5.3 Bond Distance (Å) and Bond Strength (valence units) in Refined Cancrinite

Bond		Distance(Å)		Bond Strength (v.u.)	
				a	b
Al-O(1)		1.728(3)		0.823(7)	0.762(5)
-O(2)		1.717(3)		0.849(7)	0.783(5)
-O(3)		1.741(3)		0.793(6)	0.738(5)
-O(4)		1.747(3)		0.779(6)	0.727(5)
	Mean	1.733	Total	3.244(14)	3.011(11)
Si-O(1)		1.608(3)		1.048(08)	1.038(8)
-O(2)		1.601(3)		1.069(12)	1.057(11)
-O(3)		1.619(4)		1.017(14)	1.008(13)
-O(4)		1.621(3)		1.011(08)	1.003(7)
	Mean	1.612	Total	4.146	4.106(20)
$Na_2(Ca)$-O(1)		2.507(3)		0.146(0)	0.154(0)
-O(3)		2.427(4)		0.175(1)	0.177(1)
-O(3)		2.859(3)		0.070(0)	0.088(0)
-O(4)		2.444(3)		0.168(1)	0.172(0)
-O(4)		2.891(6)		0.066(0)	0.084(0)
-O(51)		2.411(11)		0.181(4)	0.183(3)
-O(51)		2.432(20)		0.173(7)	0.176(6)
-O(51)		2.441(11)		0.169(4)	0.173(3)
	Mean	2.552	Total	1.146(10)	1.208(8)

Table 5.3 (Cont'd.)

Bond		Distance(Å)	Bond Strength (v.u.)	
			a	b
$Na_2(Ca)$-O(1)		2.507(3)	0.146(0)	0.154(0)
-O(3)		2.427(4)	0.175(1)	0.177(1)
-O(3)		2.859(3)	0.070(0)	0.088(0)
-O(4)		2.444(3)	0.168(1)	0.172(0)
-O(4)		2.891(6)	0.066(0)	0.084(0)
-O(52)		2.413(13)	0.180(5)	0.182(4)
-O(52)		2.424(21)	0.176(8)	0.178(6)
-O(52)		2.433(11)	0.172(4)	0.176(3)
	Mean	2.550	Total 1.152(11)	1.212(8)
Na(1)-O(6)		2.875(15)	0.068(2)	0.086(1)
-O(6)		2.3 9(15)	0.215(7)	0.208(5)
-O(1)*3		2.864(3)	0.207(0)	0.261(0)
-O(2)*3		2.451(3)	0.495(1)	0.510(0)
	Mean	2.633	Total 0.985(5)	1.065(3)
Ca(1)-O(6)		2.875(15)	0.100(3)	0.086(1)
-O(6)		2.339(15)	0.345(13)	0.208(5)
-O(1)*3		2.864(3)	0.306(0)	0.261(0)
-O(2)*3		2.451(3)	0.783(1)	0.510(0)
			Total 1.534(9)	1.065(3)

Further evidence that the cage doesn't contain calcium (labelled Ca(1) in Table 5.3) in the place of sodium (Na(1)) is provided from bond strength calculations. Set 'b' curve indicates a valence of 1.5 (0.75 Ca) and set 'a' curve a valence of 1. (0.5 Ca) instead of the 2 valence required for calcium. The latter value is possible but there is no physical reason why. Nevertheless, if Ca were in the cages, there would be considerable charge balance deficiency in the large channels.

CHAPTER 6

THE SUBMICROSTRUCTURE OF CANCRINITES

Even though a well refined average structure for cancrinite is now determined, the precise cause of the superstructure maxima remains to be defined. X-ray diffraction may not provide this information as X-ray data is averaged over thousands of unit cells and assume that the cells are identical. Thus one must seek other evidence. At the initial stage of this study, it was hoped that HRTEM studies could be successful in locating the positions of the calcium atoms since they are twice as good a scatterer as sodium. Also, if stacking faults are present, they could easily be imaged. However, as the results indicated, there are no stacking faults and calcium positions could only be identified on the c-axis projection, not the a*-c* projection which is more desirable.

Both XRD and HRTEM indicates that the framework and the cages are well defined and ordered. Consequently, the cause of the superstructure maxima is in the large channels and are due to the intra-framework ions in that channel.

Chemical analyses of $(Na,Ca)CO_3$ cancrinites from different localities (to be discussed in section 6.4) consistently shows a deficiency of $CaCO_3$. The way(s) in which Ca^{2+} and CO_3^{2-}, together with the vacant sites, are distributed is unknown. However, the electron diffraction patterns of the a*-c* reciprocal lattice (and corresponding electron images) show that the superstructure maxima are quite regular.

This suggests that the distribution of the ions and vacant sites in the large channels are quite regular.

6.1 Superstructure Instability:

Diffraction patterns show that all reflections are initially of moderately strong intensity and the intensity within each reflection row is about equal. After a few minutes of exposure to a 100 kV electron beam, the superlattice reflections become progressively less intense, and they streak and eventually become extinguished. If the specimen has not bent badly because of beam heating, the initial intensity of these reflections mean that the atoms giving rise to the superlattice reflections are in well defined sites (partial ordering). Exposure to high energy and high frequency radiation produces displacement, an elastic effect which ejects atoms from the crystal and progressively destroys the order.

Foit et al. (1973) studied the behaviour of the superstructure reflection intensity as a function of temperature. They show that, there were no significant variations in substructure intensities with increasing temperature but the superstructure intensities decrease considerably. Substructure intensities return to their original values upon cooling the crystal, but superstructure intensities, although increasing with decreasing temperature, returned to only a fraction of their original values and at the same time, they are much more diffuse, relative to substructure intensities. These authors attribute the decrease in superstructure intensity as loss of H_2O. Chen (1970) suggest that both CO_2 and H_2O are lost on heating. The water is strongly bonded to the cations in the cages and thus it is more likely CO_2 is lost on

heating and as will be shown later, it is the $CO_3^{=}$ that is responsible for the superstructure reflections. It is interesting to note that Kozu (1931) (in Deer et al. 1963) observed that the loss of weight curve of a cancrinite (Table 6.2, anal. 2) shows breaks at 300°C and 400°C, and interpreted these breaks as due to loss of carbon dioxide.

Chen (1970) also shows that when the heated crystals are quenched to room temperature, the positions of superstructure reflections shift towards the origin that is, the superstructure spacings increase with increasing temperature. Since CO_2 is lost on heating, the remaining carbonate ions would re-order differently and since the amount is less, they must order themselves over a greater distance.

6.2 Model for the Superstructure in Cancrinite

No present model can adequately describe the superstructure in cancrinite. The diffraction image of cancrinite may be the result of a simple harmonic structural perturbation in the c-axis direction (Jarchow, in Foit et al. 1973). Description of the structure as normal (unmodulated) based on some supercell presumably cannot be exact, since such a description is in conflict with the continuous change of the superstructure maxima in reciprocal space, with temperature (Dubbeldam and DeWolff, 1969).

Modulated structures can occur as substitutional type i.e. ordering of substituting atoms and/or defects, such as described recently by Sadanaga et al. (1978) who described the superstructures of sulfides (pyrrhotite and the minerals belonging to the bornite-digenite join) and silicates (intermediate plagioclase, mullite and hauyne). It should be

noted that the sulfides are grossly defective nonstoichiometric compounds, as is cancrinite.

Dubbeldam and DeWolff (1969) described the superstructure of γ- Na_2CO_3 (perfect stoichiometry) as ordering of the anion orientation. However, DeWolff group (Van Aalst et al. 1976) later described this superstructure as a harmonic displacive modulation (displacement modulation). In cancrinite, such a displacement modulation of the CO_3 ion seem hardly possible since the CO_3 ion is "locked" in specific orientation by the surrounding Na(Ca) cations.

The superstructure in cancrinite if it is modulated, seems most likely to be that of the substitutional type, similar to that of the sulfides. Consequently, we are concerned with the orientation and positions of the CO_3 ion, and its vacancies and to a lesser degree, cations and their vacancies. Before this is examined, the superstructure spacings themselves need to be reexamined in detail.

NC-values for a few cancrinites were given in Table 4.1. Table 6.1 includes these NC-values together with additional data for cancrinites from different sources. In Table 6.1, NC-values for the various samples are listed so that '---' corresponds to the reflections not observed when the reflections are indexed on some multiple subcell. Upon cursory examination of the NC-values, the superstructures of cancrinites seem to be incommensurate and thus modulated. However, if one considers that the NC-values for any one cancrinite as part of a series of reflections that can be expressed as a simple fraction of the interval between the main reflections, then the NC-values agree quite well with a supercell that is an <u>exact</u> multiple of the subcell. This is clearly shown in Table 6.2.

TABLE 6.1: Summary of values of 'cancrinites' superstructures

	Sample Locality	C_0	N_1C	N_2C	N_3C	N_4C	N_5C	N_6C	N_7C	N_8C	N_9C	$N_{10}C$	$N_{11}C$	$N_{12}C$	$N_{13}C$	$N_{14}C$	$N_{15}C$	$N_{16}C$	Author/ Method
1.	Mandaoria,* Inde. BM No. 1930-115	5.12	25.60	12.80	8.36	6.50	(5.12)												Brown & Ossaboa (1973) XRD
2.	Princess Quarry,* Bancroft, Ont.	5.12	33.28	---	11.75	8.68	---	6.05	(5.12)										Brown & Ossaboa (1973) XRD
3.	Litchfield, Maine, U.S.A.	5.14	---	---	12.0	---	---	---	(5.14)										Jarchow (1965) XRD
4.	Mathuen Tp. Ont. (67001)	5.13	---	---	---	9.2	---	---	(5.13)										Chen (1970) XRD
5.	Mathuen Tp. Ont. (69008)	5.12	---	---	---	9.2	---	---	(5.12)										Chen (1970) XRD
6.	Dungannon Tp. Ont. (68024)	5.13	40.96**	20.50	13.60	---	8.1	---	---	(5.13									Chen (1970) XRD
7.	Dungannon Tp. Ont. (68024)	5.12	40.96	20.37	13.56	---	8.24	6.86	5.87	(5.12									This study EM
8.	Bancroft, Ont.	5.13	---	---	---	14.1	---	---	---	---	---	---	(5.13)						Foit et al. (1973) XRD
9.	Dungannon, Tp. Ont. (67002)	5.13	---	---	---	17.8	14.4	---	---	---	7.9	---	---	---	---	(5.13)			Chen (1970) XRD
10.	Kishengarh,* Inde. BM No. 1930-116	5.12	---	36.31	24.49	---	13.77	---	---	8.68	---	6.89	---	6.05	---	(5.12)			Brown & Ossaboa (1973) XRD
11.	Iron Hill,* Colorado	5.12	---	40.96	---	---	---	---	11.70	---	9.31	---	---	---	---	5.94	---	(5.12)	Brown & Ossaboa (1973) XRD

* Re-measured by author

** Found by author

Table 6.2 Comparison of observed and calculated superstructure spacings based on multiple subcells. (Mineral numbers are the same as for Table 6.1)

Supercell/ Superstructure Reflections	Calculated Superstructure Spacings	Sample No. / observed superstructure Spacings		
$5c_o$		1.		
hk1	25.60	25.60		
2	12.80	12.80		
3	8.53	8.36		
4	6.50	6.50		
5	5.12(Main)	(Main)		
$7c_o$		2.	3.	4,5
hk1	35.84	33.28	---	---
2	19.72	---	---	---
3	11.95	11.75	12.0	---
4	8.96	8.68	---	9.2
5	7.17	---	---	---
6	5.97	6.05	---	---
7	5.12(Main)	(Main)	(Main)	(Main)
$8c_o$		6.	7.	
hk1	40.96	40.96	40.96	
2	20.48	20.50	20.37	
3	13.65	13.60	13.56	
4	10.24	---	---	
5	8.19	8.1	8.24	
6	6.83	---	6.86	
7	5.85	---	5.85	
8	5.12(Main)	(Main)	(Main)	

Table 6.2 (cont'd.)

Supercell/ Superstructure Reflections	Calculated Superstructure Spacings	Sample No. / observed superstructure Spacings	
$11c_o$		8.	
hkl	56.52	---	
2	28.16	---	
3	18.77	---	
4	14.08	14.1	
5	11.26	---	
6	9.39	---	
7	8.05	---	
8	7.04	---	
9	6.25	---	
10	5.63	---	
11	5.12(Main)	(Main)	
$14c_o$		9.	10.
hkl	71.68	---	---
2	35.84	---	36.31
3	23.89	---	24.49
4	17.92	17.8	---
5	14.34	14.4	13.77
6	11.95	---	---
7	10.24	---	---
8	8.96	---	8.68
9	7.96	7.9	---
10	7.17	---	6.89
11	6.52	---	---
12	5.97	---	6.05
13	5.51	---	---
14	5.12(Main)	(Main)	(Main)

.../

Table 6.2 (Cont'd.)

Supercell/ Superstructure Reflections	Calculated Superstructure Spacings	Sample No. / observed superstructure Spacings
$16c_o$		11.
hk1	81.96	---
2	40.96	40.96
3	27.31	---
4	20.48	---
5	16.38	---
6	13.65	---
7	11.70	11.70
8	10.24	---
9	9.10	9.31
10	8.19	---
11	7.45	---
12	6.83	---
13	6.30	---
14	5.85	5.94
15	5.46	---
16	5.12(Main)	(Main)

Hence, the superstructures for cancrinites are commensurate and thus unmodulated. The fact that only certain reflections of the series of reflections for any multiple cell are observed, does not mean that the others are non-existent. On the contrary, they may be very weak and cannot be observed easily. In fact, Brown and Cesbron observed all the reflections for cancrinite -- Mandaoria, Inde (BM no. 1930.115) based on a $5c_o$ supercell. Moreover, after this theory was developed, the author looked carefully at Chen's (1970) precession photographs and electron diffraction patterns of this study and found two additional superstructure reflections for cancrinite (68024) that corresponds to 40.96Å (Chen, 1970-Plate 4) and 5.85Å. Figure 6.1 shows both of these reflections. Thus six out of seven superstructure reflections, based on an $8c_o$ supercell, were observed. Precession photographs currently being taken are confirming all of these superlattice reflections.

Table 6.2 shows that the cancrinite samples from different sources can be indexed on supercells of $5c_o$, $7c_o$, $8c_o$, $11c_o$, $14c_o$ and $16c_o$. Jarchow (1965) and Foit et al. (1973) noticed 3/7 and 4/11 fractions respectively for their superstructure reflections. Brown and Cesbron (1973) claim that sample Nos. 1, 2, 10 and 11 can be indexed on a multiple cell of $5c_o$, $16c_o$, $21c_o$ and $11c_o$ respectively. However, the superstructure spacings for these samples were remeasured by the author and they seem to correspond to $5c_o$, $7c_o$, $14c_o$ and $16c_o$ respectively.

The commensurate nature of the superstructure reflections raises an important question as to the validity of structure of recently discovered new mineral phases which have been referred to by various authors: liottite (Merlino and Orlandi, 1977a; Merlino and Mellini, 1976;

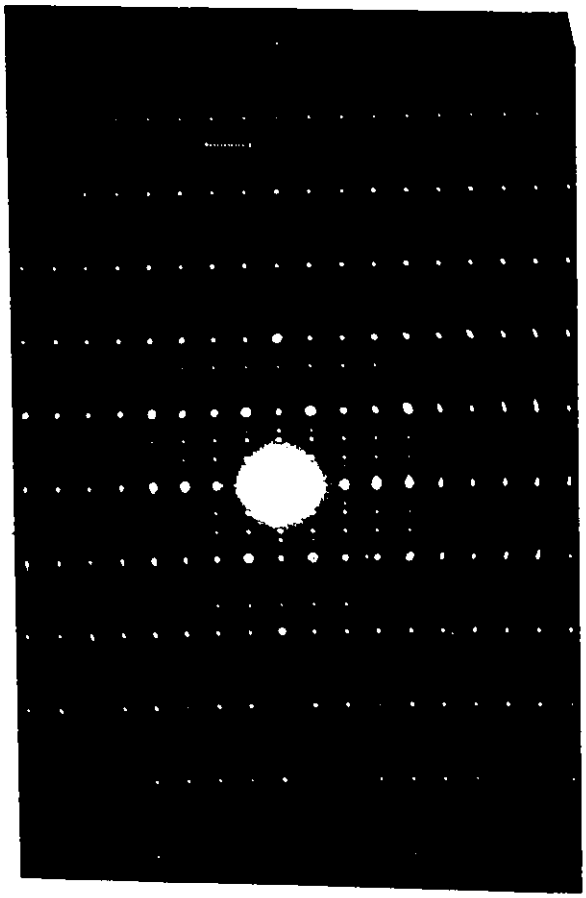

Figure 6.1: Electron diffraction pattern of cancrinite (68024) taken with the incident beam normal to the (100) plane. c* is vertical and a* is horizontal. Note the six sets of superstructure reflections: 002, 003, 005, 006, 007 and 009. In particular, 007 and 009 which corresponds to 5.85Å and 40.96Å respectively, as they are not seen in Figure 4.2.

Rinaldi and Wenk, 1979); afghanite (Bariand et al., 1968; Merlino and Mellini, 1976; Rinaldi and Wenk, 1979); franzinite (Merlino and Orlandi, 1977b; Rinaldi and Wenk, 1979; Merlino and Mellini, 1976); and possibly also microsommite (Klaska and Jarchow, 1977); and "Losod" (Sieber and Meier, 1974). With the exception of microsommite, whose a-dimension is twice that of cancrinite, all the other minerals mentioned have the same a-dimensions as cancrinite but their c-dimensions are integral multiple of cancrinite c_o-- microsommite (c_o); Losod ($2c_o$); liottite ($3c_o$); afghanite ($4c_o$); franzinite ($5c_o$). This fits elegantly with the model of commensurate superstructures for cancrinite. Consequently, what are being considered as 'main' reflections by the various authors who studied these new mineral phases are in fact superstructure reflections of cancrinite proper (superlattice data is not available for microsommite nor losod as yet and speculations are not strictly applied to these two minerals). As a result of considering the new minerals as being different from cancrinite, some very complicated stacking sequences had to be proposed (Table 1.1). The very nature of these complications would suggest that they are not valid framework structures.

Furthermore, different stacking sequences for these minerals would seem unlikely to eliminate superstructures of the cancrinite type. Wenk (1978) published the lattice fringe images of afghanite (see Plate 1) and referred to the 43Å and 64Å fringes as superstructures of corresponding magnitudes. However, Rinaldi and Wenk (1979) diffraction patterns of afghanite (Plate 1) does not show any "superstructure reflections" that corresponds to such periodicities. These authors noted that the 42Å and 64Å repeats were found in local areas. Thus it

seems likely that these repeats correspond to entirely different phases that may not be related to franzinite, liottite or afghanite. The electron diffraction patterns of these new mineral phases (Plate 1) have quite regular intensities with the exception of franzinite. However, electron diffraction patterns of cancrinite (Fig. 4.2) also show regular intensities for the superstructure reflections but x-ray precession photographs (Chen, 1970; Foit et al., 1973; Brown and Cesbron, 1973) show that these intensities are irregular. The physics of electron diffraction is very complicated and it is much easier to compare intensities obtained by XRD methods. To the author's knowledge, only one x-ray photograph has been published by Bariand et al. (1968) for afghanite. This photograph clearly shows that the reflections that are being considered as 'main' reflections by Rinaldi and Wenk (1979) are in fact superstructure reflections that are very similar to those of cancrinite. Therefore, liottite, afghanite and franzinite are cancrinite proper.

Losod is possibly the same in this respect as it can be indexed on a $2c_o$ subcell, but superstructure data is needed to define the superlattice. In addition, Microsommite is related to the cancrinite cell by $a = 2a_o$; $c = c_o$. The doubling of the a-dimension seems to indicate that adjacent channels are different in terms of the ordering of the same or different chemical constituents it contains. Therefore, it seems likely that the framework of microsommite is the same as cancrinite. Here again, further work needs to be dome on microsommite as superstructure data is not yet available.

To summarize, all the new mineral phases have the same framework structure as cancrinite. They differ from each other in terms of ordering of the same or different anions in the large channels which in turn are responsible for their different commensurate superstructures. This should clearly be reflected in the chemistry of these phases. However, before this is done, it is necessary to show that the ordering of the anions in the large channels are responsible for the superstructure reflections.

6.3 Structure factor calculation for superlattice reflections for a $(Na,Ca)CO_3$ Cancrinite.

Based on the model of multiple subcell, structure factor (FC) calculation was attempted to reproduce the intensities of the superlattice reflections for cancrinite (68024). The multiple subcell for this sample is $8c_o$. Due to the high symmetry of the CO_3 group and its vacant sites, calculations were done only for the $00l$ reflections using only the atoms of the CO_3 group as they are believed to be the major cause of the superstructure reflections.

Intensity of the form

$$F^2_{hkl} = [\Sigma f_j \exp i\, 2\pi(hx_j + ky_j + lz_j)]^2$$

was used and it was corrected for Lorentz and polarization for precession photographs taken with $\mu = 30^\circ$ (zero level).

Since the CO_3 group is considered to be the major contributor to the superstructure reflections, they were positioned in such a way as to give a $8c_o$ repeat, with due consideration for the chemistry. The average structure shows that there are two equally probable positions

for the CO_3 groups. If the C1 site is represented by x and the C2 site by 0, then Figure 4.2 shows the positions of the CO_3 ions in a $8c_o$ supercell. In this figure, a filled site is represented by C1 or C2. This arrangement of the CO_3 ions accounts well for its chemistry (1.625-model vs 1.57 or 1.62-duplicate analyses).

Intensities for the 00ℓ reflections are given in Table 6.3. The intensities were not corrected for temperature factor (isotropic) since at small values of $\sin\theta/\lambda$ the correction terms were close to unity. The values for the intensities were rounded to the nearest 100. All necessary data for the calculations were taken from: International Tables for X-ray Crystallography.

Of the 00ℓ reflections, only three reflections (00,13; 00,27; 00,29) are seen on precession photographs (Chen, 1970). The other 00ℓ reflections are either blocked by the beam stop or are covered by streaking of the main reflections. However, reflection 00,13 is very strong and this is clearly confirmed by the calculation. Reflections 00,27 and 00,29 are moderately strong and they are about equal intensity. This is also confirmed by the calculation.

The calculation seem to confirm the observed intensities in a general way. However, if the Na_2 (Ca) atoms in the large channels do not strictly confirm to $P6_3$ symmetry then these atoms would modify the calculated intensities. From consideration of the temperature factor of these cations, it would seem that they are possibly positionally disorder. Nevertheless, since the intensity of 00,13 is so strong, it is not likely that the Na_2(Ca) atoms would affect this reflection to any great degree.

Figure 6.2: Arrangement of CO_3 ions in a $8c_o$ supercell. Filled sites are represented by C1 or C2. (x = C1 site; 0 = C2 site; diagram is not to scale).

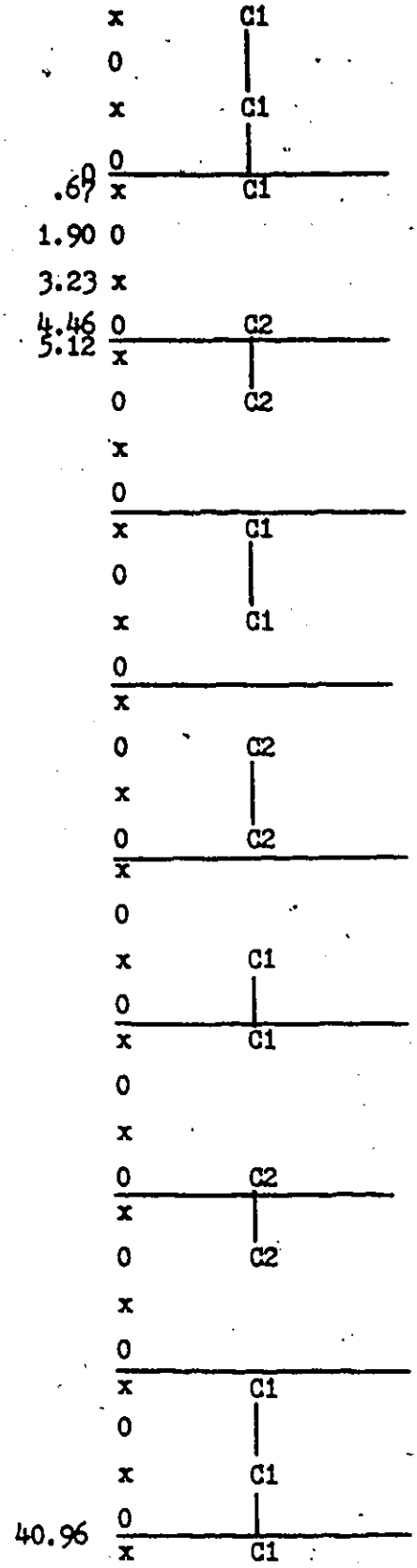

Table 6.3: Calculation of 00ℓ reflections based on the CO_3 group positioned as in Figure 6.1

00ℓ	$d_{00\ell}$	$F_{00\ell}$	Visual Intensity (Chen, 1970 - photographs)
001	40.96	1300	
2	20.48	800	
3	13.65	900	
4	10.24	1200	
5	8.19	3000	
6	6.82	36400	
7	5.85	15300	
8	5.12	2900	
9		1600	
10		1600	
11		2000	
12		8500	
13		126800	VVS
14		3900	
15		1100	
16		1300	
17		1000	
18		2200	
19		45600	
20		2700	
21		600	
22		300	
23		200	
24		300	
25		1200	
26		2000	
27		100	MS
28		00	
29		200	MS
30		00	
31		00	
32		20111	

Similar calculation can be made to account for the cancrinites showing different subcell multiples. Essentially, one needs to position the vacant anion sites as equally spaced as possible and to have the appropriate multiple cell repeat. It should not be assumed that Cl-Cl sandwiches are the only building unit. The model selected must give approximately equal occupancies of both C1 and C2 (44% occupancy of C1 and 38% occupancy of C2) and it must also account for the chemistry.

6.4 Chemistry of Cancrinite Minerals

Chemical analyses of cancrinite (mainly carbonate-rich) from different sources, calculated on the basis of 12(Si + Al) are given in Table 6.4. Ideally, the number of (Na + K + Ca) should be 8. There is a consistent deficiency in the sum of these cations (with the exception of analyses No. 11, synthetic sample). This suggest that cation vacancies are common in cancrinite. The number of (CO_3 + SO_4) should ideally be 2, but Table 6.4 shows that this sum (with the exception of analysis 10) is less than 2.0, suggesting that some of these anion sites are vacant. Furthermore, the total amount of water in nearly one-half the number of analyses, show an excess of H_2O over the ideal value of 2, which indicates that water is filling the sites of cation vacancies.

For completeness, the chemistry of the sulphatic varieties (vishnevite) and (K, Cl) varieties (microsommite or davyne) should also be considered. Table 6.5, taken from Deer et al. (1963) and Table 6.6, taken from Bariand et al. (1968) give the composition of these varieties. In general, high Ca contents are associated with high values of CO_2, whereas the more sulphatic varieties are relatively rich in sodium.

Table 6.4 Chemical Analyses of Cancrinite from different sources and localities (Number of ions on the basis of 12 (Si+Al)

	1	2	3	4	5	6	7	8	9	10	11	12	13	14	15	16	17	18	19	20
Si	5.98	6.15	5.80	5.97	6.12	6.02	6.17	6.06	6.0	6.14	6.11	5.98	6.60	6.10	5.94	6.08	6.20	5.98	5.86	5.92
Al	6.02	5.85	6.20	6.03	5.88	5.98	5.83	5.94	6.0	5.86	5.89	6.02	5.40	5.90	6.06	5.92	5.80	6.02	6.14	6.08
Na	5.96	5.79	4.66	6.37	5.26	5.48	3.32	5.48	6.3	5.15	7.70	7.17	6.77	6.38	6.66	5.86	6.27	5.10	5.19	6.31
K	.02	.21	.18	.14	.92	.03	0.27	.02	--	.05	.01	.50	.07	.02	.06	.04	.05	.18	.11	.33
Ca	1.51	.91	1.56	.90	.28	1.91	2.18	1.02	.91	1.48	.46	--	.55	.93	.97	1.09	1.29	1.46	1.61	.79
CO_3	1.57	1.31	1.42	1.68	.24	1.61	1.47	1.34	1.47	2.67	1.09	1.05	1.29	1.51	1.32	1.47	1.51	1.39	1.61	.76
SO_4	--	--	--	.18	.75	--	.03	.02	—	--	--	--	--	--	--	--	--	--	--	.61
H_2O	1.75	1.97	2.09	2.54	4.41	2.02	3.71	2.48	2.47	.15	2.29	2.30	2.96	2.16	2.99	2.96	2.52	2.10	2.68	2.91
Na+K+Ca	7.49	6.91	6.40	7.41	6.46	7.42	5.77	6.25	7.21	6.68	8.17	7.67	7.39	7.33	7.69	6.99	7.57	6.74	6.91	7.42
CO_3+SO_4	1.57	1.31	1.42	1.86	.99	1.61	1.50	1.36	1.47	2.67	1.09	1.05	1.29	1.51	1.32	1.47	1.51	1.39	1.61	1.37

Analyses No.	Author
1	Chen (1970)
2	Chen (1970)
3	Chen (1970)
4	Phoenix and Nuffield (1949) in Deer et al. (1966)
5	Zavaritsky (1929) in Deer et al. (1966)
6	Foit et al. (1973)
7	Meen (1938) in Foit et al. (1973)
8	Nithollon (1955)
9	Jarchow (1965)
10	Sokolov et al. (1977)
11	Sokolov et al. (1977)
12-20	Borgstrom (1930) in Nithollon (1955)

12 -- Synthetic Sample; 13 & 17 -- Brevig; 14 & 15 -- Litchfield; 16 -- Miask; 18 -- French River; 19 -- Colorado; 20 -- Beaver Creek.

Locality	
68024	Dungannon Township, Ont.
67001	Blue Mt. Mathuen Township, Ont.
67002	Dungannon Township, Ont.
	Blue Mt. Ont.
	Ilmen Mt. U.S.S.R.
	York River, Bancroft, Ont.
	Davis Quarry, Bancroft, Ont.
	Litchfield, U.S.A.
	Litchfield, U.S.A.
	Unknown locality, natural sample.
	Synthetic Sample.

Table 6.5: (Taken from Deer et al. 1963).

	Cancrinite and			
	1.	2.	3.	4.
SiO_2	33·64	35·22	35·38	33·98
TiO_2	0·07	—	—	—
Al_2O_3	29·82	29·79	28·42	29·11
Fe_2O_3	—	tr.	—	—
FeO	—	—	—	—
MnO	—	—	—	—
MgO	0·29	0·05	—	—
CaO	5·64	5·17	11·68	4·80
Na_2O	16·41	16·16	9·82	16·69
K_2O	0·50	0·17	1·22	0·81
H_2O^+	4·61	2·73	6·29	4·34
H_2O^-		—	0·60	0·23
CO_2	5·79	5·88	5·18	7·00
SO_2	0·03	0·08	0·19	1·37
Cl	tr.	0·03	0·08	0·42
	99·90	100·28	99·95	100·58
O≡Cl	—	—	0·02	0·10
Total	99·90	100·28	99·93	100·48
ϵ	1·501	1·5015	1·503	1·495
ω	1·524	1·5238	1·528	1·515
δ	0·023	0·022	0·025	0·019
D	2·51	2·44	2·476	2·422
	Numbers of ions on			
Si	5·987 } 12·00	6·007 } 12·00	6·164 } 12·00	5·971 } 12·00
Al	6·130	5·990	5·838	6·033
Ti	0·009 } 7·05	— } 7·55	— } 5·77	— } 7·42
Fe^{+3}	—	0·000	—	—
Mg	0·102	0·012	—	—
Fe^{+2}	—	—	—	—
Mn	—	—	—	—
Na	5·210	6·001	3·316	6·288
Ca	1·614	1·493	2·177	0·906
K	0·111	0·036	0·274	0·114
H_2O	2·682	1·553	3·714	2·544
C	1·617 } 1·62	1·359 } 1·39	1·470 } 1·52	1·679 } 1·93
S	0·006	0·010	0·025	0·180
Cl	0·000	0·008	0 023	0·125
100C:(C+S)	99·7	99·3	95·3	90·7

1. Cancrinite, associated with monticellite and melanite in vein, Iron Hill, Gunnison County, Colorado (Larsen and Foshag, 1920). Anal. W. F. Foshag.
2. Cancrinite, sodalite–nepheline-syenite, Dôdô, Kôgendô, Korea (Kôzu, 1931). (Average of analyses by K. Seto and S. Tuzuki.)
3. Cancrinite, veins in nepheline, Bancroft, Ontario (Moen, 1938). Anal. V. B. Moen.
4. Cancrinite, Blue Mountain, Methuen township, Ontario (Phoenix and Nuffield, 1949). Anal. R. Phoenix.

Vishnevite analyses					
5.	6.	7.	8.	9.	
33·70	35·40	34·76	35·29	34·53	SiO_2
—	0·00	—	—	0·10	TiO_2
29·40	29·78	30·61	28·79	29·06	Al_2O_3
—	0·05	—	0·19	0·56	Fe_2O_3
—	0·42	—	—	0·11	FeO
—	0·00	—	—	0·09	MnO
—	0·13	—	0·10	0·09	MgO
4·18	1·12	3·87	1·49	1·48	CaO
16·52	20·77	18·90	16·85	16·51	Na_2O
1·46	0·96	1·29	4·15	5·11	K_2O
4·24	4·17	2·30	7·62	5·35	H_2O^+
0·72	0·00	0·20	—	1·38	H_2O^-
2·18	2·18	1·90	1·01	0·28	CO_2
4·65	4·70	5·93	5·78	5·02	SO_2
—	0·35	—	—	0·09	Cl
100·12	100·01	100·28	100·05	100·02	
—	0·08	—	—	0·02	O≡Cl
100·12	99·93	100·28	100·05	100·00	Total
1·500	1·483	1·497	n1·492–1·483	—	ϵ
1·509	1·499	1·502	—	1·489	ω
0·009	0·008	0·005	—	±0 001	δ
2·443	2·402	2·42	2·35	2·328	D
the basis of 12(Si+Al)					
5·916 } 12·00	6·025 } 12·00	5·868 } 12·00	6·118 } 12 00	6·022 } 12·00	Si
6·086	5·976	6·129	5·886	5·976	Al
— } 7·42†	0·000 } 7·37	— } 7·19‡	— } 6·81	0·012 } 6·87	Ti
—	0·006	—	0·025	0·074	Fe^{+3}
—	0·023	—	0·026	0·023	Mg
—	0·059	—	—	0 016	Fe^{+2}
—	0·000	—	—	0·014	Mn
6·302	6·554	6·182	5·260	5·532	Na
0·786	0·206	0·700	0·277	0·277	Ca
0·225	0 208	0·278	0·919	0·569	K
2·483	2·368	1·295	4·408	3·112	H_2O
0·762 } 1·38	0·502 } 1·20	0·436 } 1·19	0·239 } 0·99	0·062 } 0·85	C
0·613	0·600	0·751	0·749	0·764	S
—	0·101	—	—	0·026	Cl
55·4	45·6	26·8	24·2	7·8	100C:(C+S)

5. Sulphatic cancrinite, Iron Hill, Gunnison County, Colorado (Larsen and Steiger, 1916). Anal. G. Steiger (Includes SrO 0·06).
6. Carbonate vishnevite (sulphatic cancrinite), cancrinite ijolite, Iivaara, Kuusamo, Finland (Lehijärvi, 1950). Anal. M. Lehijärvi.
7. Carbonate vishnevite (sulphatic cancrinite), Loch Borolan, Assynt, Scotland (Stewart, 1941). Anal. F. H. Stewart (Includes SrO 0·22).
8. Carbonate vishnevite (sulphatic cancrinite), small pests and veinlets in nepheline in pegmatite in nepheline-syenite, Ilmen mountains, U.S.S.R. (Zavaritsky, 1929). Anal. Y. V. Morachevsky.
9. Vishnevite, Vishnevy Gory, Urals (Beliankin, 1944) (Includes S 0·30).

† Includes Sr 0·008. ‡ Includes Sr 0·031.

Table 6.6: (Taken from P. BARIAND, F. CESBRON ET R. GIRAUD, 1968).

TABLEAU 6.6a

Analyses chimiques de davyne et nombre d'ions sur la base de 12 (Si + Al).

	1		2		3		4		5		6	
SiO_2....	32,21		32,38		31,94		32,23		33,12		31,40	
Al_2O_3..	29,22		28,64		28,18		28,98		28,60		27,80	
CaO...	12,60		10,55		10,23		10,36		9,91		13,82	
Na_2O..	10,14		10,74		11,85		11,01		7,22		9,07	
K_2O...	6,79		6,44		7,84		7,11		11,91		6,07	
Cl.....	5,71		7,14		7,04		6,95		5,14		5,19	
SO_3....	4,43		4,03		3,69		4,11		2,38		8,78	
CO_2....	—		1,63		1,47		1,26		2,88		—	
	102,10		101,55		102,24		102,01		101,16		102,13	
O = Cl.	— 1,51		— 1,61		— 1,59		— 1,56		— 1,16		— 1,17	
Total..	100,59		99,94		100,65		100,45		100,00		100,96	
Si....	5,800	12	5,874	12	5,884	12	5,825	12	5,946	12	5,871	12
Al...	6,200		6,126		6,116		6,175		6,054		6,129	
Ca...	2,431		2,051		2,017		2,006		1,907		2,769	
Na...	3,539	7,530	3,777	7,318	4,228	8,086	3,558	7,503	2,513	7,149	3,288	7,505
K....	1,560		1,490		1,841		1,639		2,729		1,448	
Cl. ..	2,047		2,195		2,196		2,129		1,564		1,645	
S....	0,598	2,645	0,548	3,147	0,510	3,075	0,557	2,997	0,321	2,591	1,232	2,877
C....	—		0,404		0,369		0,311		0,706		—	

1. Davyne, Monte Somma ; A. Scacchi (1876).
2, 3, 4. Davyne, Monte Somma ; H. Rauff (1878).
5. Davyne, Monte Somma ; H. Traube (1895).
6. Davyne, Vésuve ; F. Zambonini (1910).

Composition moyenne :
$(Na_{3,53}Ca_{2,29}K_{1,78})(Si_{5,87}Al_{6,13}O_{23,9})[Cl_{1,58}(SO_4)_{0,62}(CO_3)_{0,30}]$
où $(Na, Ca, K)_{7,8}(Si, Al)_{12}O_{24}(Cl, SO_4, CO_3)_{2,8}$.

TABLEAU 6.6b

Analyses chimiques de microsommite et nombre d'ions sur la base de 12 (Si + Al).

	1		2		3		4		5		6	
SiO_2...	33,0		32,12		30,74		31,40		31,70		30,95	
Al_2O_3..	29,0		29,07		31,57		30,37		32,07		31,75	
CaO....	11,2		11,19		10,77		10,84		14,72		14,68	
Na_2O...	8,7		9,89		8,46		9,75		12,45		7,18	
K_2O...	11,5		6,38		8,97		8,36		4,27		11,32	
Cl.....	9,1		8,17		7,65		7,64		6,99		5,30	
SO_3....	1,7		6,04		5,17		4,57		—		—	
	104,2		102,86		103,33		102,93		102,20		101,18	
O = Cl.	—2,05		— 1,84		— 1,73		— 1,72		— 1,58		— 1,20	
Total..	102,15		101,02		101,60		101,21		100,72		99,98	
Si...	5,893	12	5,806	12	5,428	12	5,607	12	5,473	12	5,432	12
Al..	6,107		6,194		6,572		6,393		6,527		6,368	
Ca...	2,144		2,167		2,038		2,074		2,722		2,760	
Na..	3,012	7,777	3,465	7,103	2,896	6,955	3,375	7,354	4,166	7,828	2,443	7,737
K...	2,621		1,471		2,021		1,905		0,940		2,534	
Cl...	2,754	2,982	2,503	3,322	2,280	2,974	2,312	2,924	2,045	2,045	1,576	1,576
S....	0,228		0,810		0,685		0,612		—		—	

1. Microsommite, Vésuve ; G. von Rath (1873).
2, 3, 4, 5, 6. Microsommite, Vésuve ; A. Scacchi (1875).

Composition moyenne :
$(Na_{3,51}Ca_{2,33}K_{1,93})(Si_{5,81}Al_{6,19}O_{24})[Cl_{2,23}(SO_4)_{0,30}]$
où $(Na, Ca, K)_{7,8}(Si, Al)_{12}O_{24}(Cl, SO_4)_{2,8}$.

The sulphatic varieties has a significantly lower number of (Na + Ca + K) ions and a correspondingly smaller number of (CO_3 + SO_4) anions per formula unit than the carbonate rich members. Thus in vishnevite, more of the cation and anion sites in the large channels are vacant and this also account for the lower density. This is to be expected since the CO_3 ion is planar while the SO_4 ion is tetrahedral and so the latter occupies more space.

Vishnevite contains more K than carbonate-rich cancrinite and also the former contains some chlorine. In this respect, vishnevite is more closely related chemically to microsommite than to carbonate-rich cancrinite. Chlorine is the dominant anion in microsommite and also there is a significant increase in K for this mineral.

The microsommite analyses (Table 6.6) show that there is virtually no water. The water which is in the cages for cancrinite plays an important role in the coordination of the cations in the cages. Since water is absent in microsommite, chlorine must occupy that site. Consequently, for microsommite, the excess chlorine atoms over 2.0 is the amount that remains to be placed in the large channels. Table 6.6a shows that the amount of chlorine in all the samples is less than or close to two and thus there is no excess chlorine for the large channels. Where there is deficiency, it would appear that the chlorine would be randomly distributed in the cages (Anal. #5 and #6, Table 6.6a). Table 6.6b shows that a few analyses (for example, Anal. #1 and #2) indicate an excess of chlorine over 2.0. This excess chlorine in the large channels is not expected to be positioned on the 6_3 axis as this would not provide a good coordination sphere for the cations. It seems likely

that the excess chlorine is in a three-fold position similar to the oxygens of the CO_3 group.

As suggested in section 6.1, liottite, afghanite and franzinite and perhaps losod are cancrinite proper since they seem to have the same framework structure. Thus the chemistry of these minerals is compared with other cancrinites. To do this, the compositions given in Table 1.1 must be divided by the appropriate multiple of the cancrinite subcell. The resulting chemistry is given in Table 6.7. It should be noted that the compositions given in Table 1.1 includes some hydroxy ions. However, Table 6.7 does not show any hydroxy ions as it does not seem likely that the water is in this form, except for losod which seems to have both OH^- and H_2O.

In the discussion of microsommite, it was pointed out that chlorine occupies the same site as water and therefore the sum ($Cl + H_2O$) must be considered. This sum is close to 2.0 for liottite and afghanite but is less than 2.0 for franzinite. Consequently, the chlorine and water are statistically distributed over the same sites in these minerals with some sites actually vacant in franzinite or there may be partial ordering of Cl and H_2O.

Losod (synthetic sample, no natural sample is found as yet) shows an excess of H_2O over 2.0. This excess must be OH^- and they are in the large channels and possibly occupying similar sites as the oxygen of the CO_3 group. This mineral can be considered as hydroxy-cancrinite.

Liottite and franzinite have the full compliment of cations but afghanite definitely shows an excess over the ideal value of 8.0. It appears that there is no room for any excess cations and perhaps the afghanite analysis is in error.

Table 6.7: Chemical analyses of a few cancrinite-related minerals.

	Losod($2c_o$)	Liottite($3c_o$)		Afghanite($4c_o$)		Franzinite($5c_o$)	
Si	6.0	6.11	12.0	6.13	12.0	6.26	12.0
Al	5.5	5.89		5.87		5.74	
Fe^{3+}		0.05		----		0.01	
Mg		----		----		0.04	
Ca		3.59	8.01	3.52	9.06	2.50	7.89
Na	5.75	3.10		4.86		4.30	
K		1.27		0.68		1.04	
SO_4		1.30	1.87	1.27	1.38	1.54	1.95
CO_3		0.57		0.11		0.41	
Cl		0.87	2.08	1.55	2.02	0.12	1.33
H_2O	8.5	1.21		0.47		1.21	

The cation sites for cancrinite are well defined and it appears that they would be the same for all the cancrinite related minerals. However, to predict the anion sites for the cancrinite related minerals, we need data for their superstructures. This is not available for microsommite (or davyne) nor losod. Thus detail analyses of these structures beyond what have already been discussed is not necessary as yet. However, complete data is available for liottite, afghanite and franzinite and for these, only the CO_3 and SO_4 positions remain to be predicted. On the basis of theoretical considerations of the SO_4 group, it can easily be seen that the maximum amount of SO_4 that can be accommodated by the cancrinite structure is 1.33, which indicates that the SO_4 determination for franzinite is in error.

As was done for the carbonate-rich cancrinite, the arrangement of SO_4 and CO_3 for liottite only will be considered, as similar ordering can be determined for afghanite and franzinite. Figure 6.3 shows the ordering pattern of these anions in the large channel of liottite. In this figure, the "basal" oxygens of the SO_4 group are positions in the planes of the C1 and C2 sites. However, to accommodate the CO_3 group, the SO_4 groups must be displaced in the directions of the arrows. This displacement is about 0.5Å. The calculated chemistry compared with the chemical analyses (Fig. 6.3) agree quite well with each other, for this ordering pattern.

In this ordering of the SO_4 and CO_3 ions, no apparent anion sites are vacant. Consequently, more regular superstructure reflections and higher intensities are seen for these minerals. As mentioned before,

Figure 6.3: The arrangement of SO_4 and CO_3 in liottite to give a $3c_o$ multiple subcell. The arrows show the direction of displacement (~0.5Å) of the SO_4 ions to accommodate the CO_3 groups. (Diagram is not scaled).

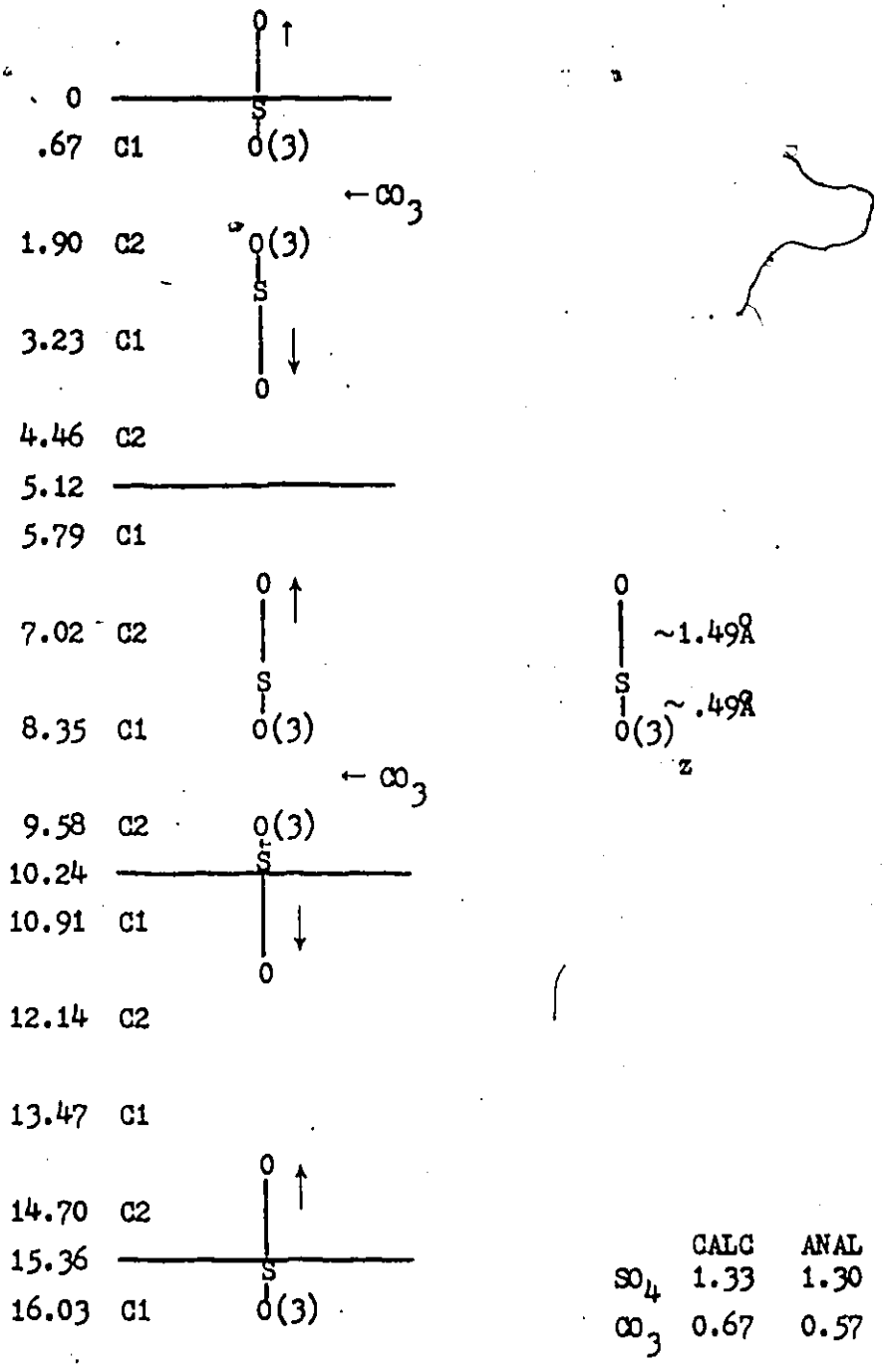

	CALC	ANAL
SO_4	1.33	1.30
CO_3	0.67	0.57

this observation has been misinterpreted by the authors who studied these minerals in that they consider the superstructure reflections as 'main' reflections. As a result, complicated stacking sequences had to be proposed for these minerals and consequently, the refinement of these minerals on that basis has resulted in quite large R-values (~16% for liottite and afghanite and ~27% for franzinite -- Merlino and Mellini, (1978) in Rinaldi and Wenk (1979).

Even though losod and microsommite (or davyne) has not been considered in detail, it seems likely that they fit the proposed model. It should be noted that the R-value obtained for losod is 40% (Sieber and Meier (1974), which is quite poor.

In summary, all the minerals mentioned in this report appears to have the same aluminosilicate framework structure as cancrinite and hence the same AB... stacking sequence. They differ only as regards the intraframework anions and cations. The arrangement of the anions (SO_4, CO_3 and OH) in the large channels give rise to different commensurate superstructure reflections, all of which can be indexed on various multiple subcells.

On this basis, it does not seem justifiable to name the new phases liottite, franzinite, etc. but instead they should be called by the appropriate subcell multiple -- for example $3c_o$-cancrinite for liottite, $5c_o$- cancrinite for franzinite, etc.

In general, the name "NC - cancrinite" is necessary and sufficient to describe cancrinites.

6.5 Geological Implications

The chemistry of cancrinite indicates that some of the volatile components (S_2, CO_2, HCl and H_2O) are always present in cancrinites. It seems likely that the fugacity or partial pressure of these volatile components dictates what anion would be taken up in cancrinite structure. For example, a high P_{CO_2} may result in the formation of carbonate-rich cancrinite while a high P_{H_2O} would result in the formation of hydroxy cancrinite. The variability of the superstructure reflections may indicate the chemical and physical conditions in which a cancrinite was formed.

6.6 Conclusions

The development of HRTEM has provided a new method to study superstructures and obtain information not only of average, but also local structures. Particularly the applications of the lattice image and electron diffraction techniques have opened a new field in the study of superstructures. These techniques present information on the submicroscopic structure, which can hardly be obtained by XRD. HRTEM has provided information on the submicroscopic structure of cancrinite which assisted in determining its average crystal structure (R = 2.9%) by x-ray diffraction techniques. Furthermore, it has been shown that the framework structure of liottite, afghanite and franzinite and possibly losod and microsommite are the same as cancrinite. They differ only as regards the intraframework anions and cations. The anions are different for different cancrinites and they are ordered in different ways. As a result, they give different commensurate superstructure reflections -- all of which can be indexed on various multiple subcells.

The positions of SO_4, Cl and OH have been predicted but this remains to be confirmed by XRD. Also the variability of the superstructure reflections seem to reflect the chemical and physical conditions of formation of cancrinite.

REFERENCES

ALLPRESS, J. G. and SANDERS, J. V. (1973), The Direct Observation of the Structure of Real Crystals by Lattice Imaging. J. Appl. Cryst., 6: 165-190.

BARRER, R. M., COLE, J. F. (1970), Chemistry of Soil Minerals, Part VI. Salt entrainment by sodalite and cancrinite during their synthesis. J. Chem. Soc., 9: 1516-1523.

BARRER, R. M., COLE, J. F., VILLIGER, H. (1970), Chemistry of Soil Minerals, Part VII. Synthesis, properties and crystal structures of salt-filled cancrinites. J. Chem. Soc., 9: 1523-1531.

BARTH, T. F. W. (1932), The Structure of the Minerals of the Sodalite group. Z. Krist. 83: 405-415.

BROWN, I. D. (1976), On the Geometry of O-H...O Hydrogen Bonds. Acta Cryst. A32: 24-31.

BROWN, I. D. and SHANNON, R. D. (1973), Empirical Bond Strength-Bond Length Curves for Oxides. Acta Cryst. A29: 266-282.

BROWN, W. L. and CESBRON, F. (1973), Sur le surstructures des Cancrinites. C. R. Acad. Sci. Paris, 276, Series D, 1-4.

BUERGER, M. J. (1960), Crystal Structure Analysis. John Wiley & Sons, N.Y.

BUSECK, P. R., IIJIMA, S. (1974), High resolution electron microscopy of silicates. Am. Mineral. 59: 1-21.

CHEN, S. M. (1970), A chemical, thermogravimetric and X-ray study of Cancrinite. M.Sc. Thesis, McMaster University.

COWLEY, J. M. and IIJIMA, S. (1972), Electron microscope image contrast for thin crystals. Z. Naturforsch., 27a: 445-451.

COWLEY, J. M. and IIJIMA, S. (1976), The Direct Imaging of Crystal Structures. In: Electron Microscopy in Mineralogy (Ed. H-R Wenk) Berlin:Springer.

COWLEY, J. M. & MOODIE, A. F. (1957), Acta. Cryst. 10, 609-619.

DEER, W. A., HOWIE, R. A. and ZUSSMAN, J. (1963), Rock Forming Minerals. Vol. 4, Framework Silicates. John Wiley & Sons Inc. N.Y.

DUBBELDAM, G. C., & P. M. DeWOLFF (1969), The average structure of γ-Na_2CO_3. Acta. Cryst. B25, 2665-2667.

EDGAR, A. D. (1964), Studies on cancrinite, II -- Stability fields and cell dimensions of calcium and potassium-rich cancrinites. Can. Mineral. 8: 53-67.

EDGAR, A. D., BURLEY, B. J. (1963), Studies on cancrinites I -- polymorphism in sodium carbonate rich cancrinite-natrodavyne. Can. Mineral., 7: 631-642.

ERICKSON, H. P. and KLUG, A. (1971), Measurement and compensation of defocusing and aberrations by Fourier processing of electron micrographs. Phil. Trans. Roy. Soc. B261: 105-118.

FEJES, P. L. (1973), Ph.D. Thesis, Arizona State Univ.

FOIT, Jr., F. F., PEACOR, D. R., HEINRICH, E. W. (1973), Cancrinite with a new superstructure from Bancroft, Ontario. Can. Mineral. II, 940-951.

GOSSNER, B. and MUSSGNUG, F. (1930), Uber Davyn und scine Beziehungen zu Hauyn und Cancrinit, Z. Krist., 73; 52-60 (Min. Abst., 4, 279).

HAWTHORNE, F. C. (1973), The Crystal chemistry of the clino-amphiboles. Ph.D. Thesis, McMaster University.

IIJIMA, S., BUSECK, P. R. (1978), Experimental study of disordered mica structures by high-resolution electron microscope. Acta. Cryst., A34, 709-719.

IIJIMA, S., COWLEY, J. M., DONWAY, G. (1973), High resolution electron microscopy of tourmaline crystals. Tschermaks Mineral. Petrog. Mitt. 20: 216-224.

JARCHOW, O. (1965), Atomanordnung und Strukturverfeine-rung von Cancrinit. Zeit Kristullogr. Bd. 122, S. 407-422.

JOHNSON, C. K. (1965), ORTEP Report ORNL-3794. Oak Ridge National Laboratory, Tennessee.

KLASKA, R. & JARCHOW, O. (1977), Synthetischer Sulfat-Hydrocancrinit vom Mikrosommit-Typ. Naturwissenschaften, 64, 93.

KOZU, S., TAKANE, K. (1933), Crystal structure of cancrinite from Sodo, Korea. Proc. Imp. Acad. Tokyo, 9, 56-59, 105-108.

LYNCH, D. F., MOODIE, A. F., & O'KEEFE, M. A. (1975), n-Beab Lattice Images. V. The use of Charge-Density Approximation in the Interpretation of Lattice Images. Acta. Cryst. A31: 300-307.

MALLINSEN, L. G., JEFFERSON, D. A., THOMAS, J. M., HUTCHISON, J. L. The internal structure of nephrite: Experimental and computational evidence for the coexistence of multiple-chain silicates within an amphibole host. (To be Published).

MERLINO, S. and MELLINI, M. (1976), Crystal structures of cancrinite like minerals. Zeolite 176. An International Conference on the Occurrence, Properties, and Utilization of Natural Zeolites. Program and Abstracts. Tucson, Arizona. p.47.

MERLINO, S., ORLANDI, P. (1977a), Liottite, a new mineral in the cancrinite-davyne group. Am. Mineral., 62, 321-326.

MERLINO, S. & ORLANDI, P. (1977b), Franzinite, a new mineral phase from Pitigliano (Italy). Neyes Jahrb. Mineral. Monatsh. p.163-167.

NITHOLLON, P. (1955), Structure Cristalline de la Cancrinite. Publications Scientifiques et Techniques du Ministere de Cair France, N. T. 53, 48.

O'KEEFE, M. A., BUSECK, P. R., IIJIMA, S. (1978), Computed crystal structure images for high resolution electron microscopy. Nature, 274: 322-324.

PAULING, L. (1930), The structure of some sodium and calcium alumino-silicates. Proc. Nat. Acad. Sci., 16: 453-459.

PHOENIX, R., NUFFIELD, E. W. (1949), Cancrinites from Blue Mountain, Ontario. Am. Mineral., 34, 452-455.

RINALDI, R. and H.-R. WENK (1979), Stacking Variations in Cancrinite minerals. Acta. Cryst. A35, 825-828.

SADANAGA, R., TAKEUCHI, Y. & MORIMOTO, N. (1978), Complex Structures of Minerals Recent Prog. Nat. Sci. Jpn., 3, 141-206.

SKARNULIS, A. J. (1975), Ph.D. Thesis, Arizona State Univ.

SKARNULIS, A. J., IIJIMA, S., COWLEY, J. M. (1976), Refinement of the defect structure of '$GeN6_9O25$' by high-resolution electron microscopy. Acta. Cryst. A32, 799-805.

SOKOLOV, Y. A., GALITSKII, V. Y., LLYUKHIN, V. V., KOBYAKOV, I. B., BELOV, N. V. (1977), Study of proton-containing groups in cancrinite by the PMR method. Kristallografiya, 22, 101-105.

SIEBER, W. and MEIER, W. M. (1974): Formation and Properties of Losod, a New Sodium Zeolite. Helv. Chim. Acta, 57, 1533-1549.

VAN AALST, W., DEN HOLLANDER, J., PETERSE, W. J. A. M. and P. M. DeWOLFF, (1976), The Modulated Structure of γ-Na_2CO_3 in a Harmonic Approximation. Acta. Cryst. B32, 47-58.

VAN DER BIEST, O. and THOMAS, G. (1976), Fundamentals of Electron Microscopy. In: Electron Microscopy in Mineralogy (Ed. H-R. Wenk) Berlin: Springer.

WENK, H. R. (1978). Proc. 9th Int. Congr. Electron Microsc. Toronto, Vol. 3, pp. 404-419.

WENK, H. R. (1976): Introduction. In: Electron Microscopy in Mineralogy (Ed. H-R. Wenk). Heidelberg: Springer.

BARIAND, P., CESBRON, F. and GIRAND, R. (1968), Une nouvelle espece minerale: l'afghanite de Sar-e-Sang, Badakhshan, Afghanistan. Comparison avec les mineraux du groupe de la cancrinite. Bull. Soc. fr. Mineral Cristallogr., 91, 34-42.